Magmatic sulfide immiscibility at an active magmatic-hydrothermal system: the case of La Fossa (Vulcano, Italy)

Fulignati P.[a], Gioncada A.[a,*], Costa S.[a,b], Di Genova D.[c], Di Traglia F.[b], Pistolesi M.[a]

[a] Dipartimento di Scienze della Terra, Università di Pisa, via S. Maria, 53 56126 Pisa, Italy

[b] Dipartimento di Scienze della Terra, Università di Firenze, via La Pira, 4 50121 Firenze, Italy

[c] School of Earth Sciences, University of Bristol, BS8 1RJ Bristol, United Kingdom

* corresponding author anna.gioncada@unipi.it

Highlights

- We give evidence of sulfide-silicate melt immiscibility at La Fossa active volcano
- Sulfide melt separation occurred during the trachyte stage
- Magmatic sulfides store Cu and S in the shallow reservoir
- La Fossa is an active analogue for mineralizing magmatic-hydrothermal systems

Keywords: magmatic volatiles; magmatic sulfide; Vulcano; magmatic-hydrothermal system

Abstract

Magmatic sulfide minerals preserved in fresh volcanic rocks can be used to trace sulfur and chalcophile element evolution in magmatic systems and to constrain the potential magmatic contribution to ore-forming fluids. In this work, we present a petrographic and microanalytical study of magmatic sulfides in the products of La Fossa (Vulcano, southern Italy), an active arc-related volcano currently with a shallow acidic hydrothermal system, and discuss the results with petrological data obtained from melt inclusions. While the sulfur-rich basalts feeding the plumbing

system were oxidized and sulfide-undersaturated, as common in arc-basalts, a major event of sulfide melt separation from the silicate melt occurred at the trachytic stage, in the shallow reservoir (minimum depth based on H_2O content of melt inclusions is 1200-2200 m), promoted by the lowering of fO_2. Sulfide immiscibility was unrelated to magnetite fractionation and was encountered after a notable sulfur loss at the transition from mafic to intermediate magma composition. The late sulfide saturation implies that the silicate melt became enriched in Cu with differentiation. This is indicated by the relatively high Cu concentration in the analyzed sulfide blebs, comparable to the composition of sulfides found in other active arc volcanoes as well as in magmatic systems associated with porphyry copper mineralization. The newly reported occurrence of sulfide immiscibility in the La Fossa shallow reservoir has implications for the evolution of sulfur in the plumbing system and for the contribution of magmatic sulfur and metals to surface fumaroles, as well as to the deep hydrothermal fluids during non-eruptive periods. The results indicate that La Fossa volcano is a possible active analogue of mineralizing magmatic-hydrothermal systems.

1. Introduction

Sulfur carried by magmas plays a key role in several geological processes, which span from the climatic consequences of the huge release of volcanic gases into the atmosphere during volcanic eruptions to the genesis of magmatic-hydrothermal ore deposits. In the last decade, the scientific research resulted in an increasing awareness of the importance of magmatic sulfur in influencing metal enrichment in porphyry and related epithermal systems, and consequently their fertility (Halter et al., 2005; Nadeau et al., 2010; Wilkinson, 2013; Richards, 2015). A primary parameter governing sulfur behavior in magmas is represented by the oxygen fugacity, with the sulfur solubility in silicate melts being higher in oxidizing (S^{+6}) than in reducing (S^{-2}) conditions (Carroll

and Rutherford, 1985; O'Neill and Mavrogenes, 2002; Jugo et al., 2010). Most porphyry systems are thought to be related to oxidized parental arc magmas (Sillitoe, 2010; Richards, 2011). Reduction of oxidized arc magmas due to cooling and fractional crystallization or assimilation of reduced crustal rocks during magma differentiation (Jenner, et al., 2010; Park et al., 2015; Edmonds and Mathers, 2017) can convert the soluble sulfate in the melt to less soluble sulfide. This triggers sulfide saturation and production of an immiscible sulfide phase. The strong affinity of chalcophile and siderophile elements for the sulfide phase will cause them to be stripped from the silicate melt (Halter et al., 2005; Nadeau et al., 2010; Fontboté et al., 2017). A primary control on the extent of metal scavenging from the silicate melt is exerted by the fraction of sulfide formed (Richards, 2015; Lowczak et al., 2018).

The timing of sulfide melt immiscibility with respect to magma differentiation and, most importantly, to fluid saturation is a critical parameter in the evolution of fertile magmatic-hydrothermal systems, affecting not only whether a system is mineralized or barren but also the metal ratios of the mineralization (Halter et al., 2005; Wilkinson, 2013; Zhang and Audetat, 2017; Lowczak et al., 2018). In case of early sulfide saturation, magmas ascending to shallower levels may have ore metals sequestered (Wilkinson, 2013). On the contrary, late sulfide saturation allows the incompatible elements to become concentrated by Rayleigh fractionation prior to volatile saturation, with subsequent exsolution of an aqueous fluid phase from magma then resulting in partitioning of ore metals into the exsolved fluid (Pokrovski et al., 2013; Lowczak et al., 2018). However, early sulfide saturation may also play an essential role in the pre-concentration of ore metals at crustal levels, where they can later be released to sulfide-undersaturated magmas refilling the plumbing system or to exsolved aqueous fluids, producing anomalously metal-rich magmatic-hydrothermal fluids (Halter et al., 2005; Nadeau et al., 2010; Wilkinson, 2013; Zhang and Audetat, 2017; Fontboté et al., 2017).

Several studies focused on the role of sulfide saturation in the genesis of porphyry copper and related epithermal systems in magmatic rocks associated with mineralized or barren areas (Halter et

al., 2005; Park et al., 2015; Zhang and Audetat, 2017; Lowczak et al., 2018), and fewer works have investigated this topic in active volcanic systems (Nadeau et al., 2010; Zelenski et al., 2017; Mandan, 2017; Georgatou et al., 2018). As magmatic-hydrothermal ore deposits can be considered the extinct equivalent of active volcanic systems (Hedenquist and Lowenstern, 1994), the study of sulfide saturation and magmatic sulfide mineral composition in the products of active volcanoes can provide useful insights to volcanic and ore genesis processes.

La Fossa (Vulcano Island, southern Italy) is an active volcano characterized by a magmatic-hydrothermal system with acidic condensates that is forming residual quartz and quartz-alunite alteration without anomalous gold concentrations (Fulignati et al., 1998; Boyce et al., 2007); this alteration is similar to that which hosts subsequent mineralization related to high-sulfidation epithermal deposits (Hedenquist and Taran, 2013). The well-studied geological and magmatic evolution of La Fossa (De Astis et al., 2013 and references therein), the arc setting and the active magmatic-hydrothermal system provide an opportunity to study potentially mineralizing processes beneath arc volcanoes. At La Fossa, the products of the Palizzi eruption show evidence of magmatic sulfide immiscibility at depth, providing constraints on evolution of the magmatic-hydrothermal system. Study of the physico-chemical conditions at sulfide saturation, together with sulfide composition and timing related to volatile exsolution, allows us to explore the possible evolution of the active Vulcano magmatic complex toward a mineralized magmatic-hydrothermal system.

2. Geological and volcanological framework

The Aeolian archipelago is located at the SE edge of the Tyrrhenian Abyssal Plain and overlies a continental crust ~15-20 km thick. The volcanic arc is composed of seven islands and several seamounts active since ~1.3 Ma that form a roughly ring-shaped structure around the Marsili Basin (De Astis et al., 2000; Chiarabba et al., 2008). The volcanism of the Aeolian Islands has been related either to the rapid subduction of the Ionian slab (Barberi et al., 1973; Keller, 1980) or to the

104 passive subduction of a detached portion of the Ionian slab (Esperança et al., 1992). The volcanic
105 products belong to typical series in an orogenic setting (calc-alkaline, high-K calc-alkaline and
106 shoshonitic). A potassic series has been proposed to distinguish the high-K rocks of Stromboli and
107 Vulcano (De Astis et al., 2000; Francalanci et al., 2004).
108 Vulcano island (Fig. 1) forms, with Salina and Lipari, a NNW-SSE trending structure that intersects
109 the arc in its central sector along the Tindari-Letojanni strike slip fault system (Ventura et al.,
110 1999). The tectonic structure of the island is controlled by NW-SE and minor NNE-SSW trending
111 normal faults (Mazzuoli et al., 1995; Ventura et al., 1999; Ruch et al., 2016). The magmatic history
112 of Vulcano (review by De Astis et al., 2013) started in the southern part of the island between 120
113 and 98 ka with formation of the Vulcano Primordiale strato-cone, made up of trachybasaltic to
114 trachyandesitic lavas and pyroclastic deposits (Fig. 1a). The Vulcano Primordiale was affected by
115 volcano-tectonic collapse that formed the Caldera del Piano, a sub-circular-shaped area
116 progressively filled by lava flows and pyroclastic units between 78 and 42 ka. Towards the end of
117 this phase, the most primitive magmas on Vulcano island, the La Sommata shoshonitic basalts,
118 were erupted. Between 50 and 20 ka, volcanic activity shifted outside the caldera, resulting in
119 deposition of tephra on the western side of the island. A dome and lava flow complex, from latite to
120 rhyolite in composition, formed in the NW sector of the island between 28 and 15 ka. The complex
121 marks the western border of the Caldera de La Fossa, located in the north sector of Vulcano. The
122 depression was filled by shoshonite to latite effusive and pyroclastic units (Gioncada and Sbrana,
123 1991). A tuff cone (La Fossa) rises 391 m above sea level inside the Caldera (Fig. 1a). Formation of
124 La Fossa started at 6 ka and the last eruption occurred in 1888-90 (Frazzetta et al., 1984). The cone
125 consists of lavas and pyroclastic products ranging from latitic to rhyolitic composition with minor
126 shoshonites (Keller, 1980; De Astis et al., 1997; Gioncada et al., 2003). According to Di Traglia et
127 al. (2013), the stratigraphy of the last 1000 years of the La Fossa cone can be divided into two main
128 eruptive clusters. The eruptive period of Palizzi and Commenda is grouped into a single eruptive
129 period (*Palizzi-Commenda Eruptive Cluster*), lasting approximately 100 years during the 13th

130 century. The deposits of the Palizzi eruption (*Palizzi Eruptive Unit*) represent the oldest unit of this
131 cluster (1170±20 AD-1230±20 AD). The younger Pietre Cotte cycle, the post-1739 AD and the
132 1888-1890 AD activity form the *Gran Cratere eruptive cluster* (1444 - 1890 AD; Di Traglia et al.,
133 2013). The migration of the volcanic activity to the north formed the Vulcanello peninsula,
134 characterized by lavas and pyroclastic products ranging from shoshonitic to trachytic compositions.
135 The wide range of differentiation degree of the magmas erupted at Vulcano can be explained by
136 fractional crystallization of shoshonitic basalts and crustal assimilation (De Astis et al., 1997; Del
137 Moro et al., 1998). Magmatic differentiation occurred in a polybaric plumbing system developed
138 between 20 km (Moho) and shallow reservoirs in the upper crust, whose configuration changed
139 with time (Peccerillo et al., 2006). The sharp changes in the composition of the erupted products
140 and the evidence for magma mixing suggest that multiple shallow magma batches evolved
141 independently (De Astis et al., 2013). Additionally, the increase in K and incompatible trace
142 element concentration in the primary melts with time has been invoked to justify the higher alkali
143 content of the younger products (De Astis et al., 1997). This was confirmed by the chemical
144 composition of shoshonitic basalts trapped as melt inclusions in the products of the last eruption,
145 compared to the older La Sommata basalts (Gioncada et al., 1998; Davì et al., 2009).
146 The products which were studied here belong to the eruptive period of Palizzi (Fig. 1b). The entire
147 period produced a large volume of volcanic materials that resulted in a substantial growth in size
148 and elevation of the cone itself (Di Traglia et al., 2013). The lower part of the *Palizzi Eruptive Unit*
149 consists of planar, cross-stratified black-grey ash layers (Pal A), a rhyolitic sub-Plinian fallout layer
150 (Pal B; Fig. 2a, b) with pumiceous bombs and lapilli (Biass et al., 2016), followed by the rhyolitic
151 Commenda lava onto the west flank of the cone. The upper part of the *Palizzi Eruptive Unit* consists
152 of planar, cross-stratified black-grey ash layers (Pal C), a trachytic sub-Plinian fallout layer (Pal D)
153 bearing pumiceous bombs and lapilli (Biass et al., 2016) (Fig. 2b, c). The unit is ended by trachytic
154 lavas (Pal F, Fig. 1b). With the exception of Pal A, for which there is no direct stratigraphical and
155 chronological evidence, the *Palizzi Eruptive Unit* was emplaced after the formation of Vulcanello,

156 in the 11th to 12th centuries AD. This nearly contemporaneous activity at La Fossa cone (resurgent
157 volcano) and Vulcanello (ring fault volcano) during the last 1000 years (Di Traglia et al., 2013)
158 suggests a possible relationship between the two different post-caldera shallow storage systems, fed
159 by the same deep magmatic system (Davì et al., 2009).
160
161 **3. The La Fossa magmatic-hydrothermal system**
162
163 The surface manifestations of the La Fossa magmatic-hydrothermal system are high-temperature
164 (up to ~700°C in the early 1990s) fumaroles located in the inner part and on the northern edges of
165 La Fossa volcanic crater. The fumarolic vapors are magmatic in composition (Bolognesi and
166 D'Amore, 1993; Chiodini et al., 1995; Capasso et al., 1997). The magmatic fluids are thought to
167 originate from degassing of magma of intermediate composition at about 3-3.5 km of depth, fed by
168 volatile-rich basaltic magmas ponded at depth in the La Fossa plumbing system (Gioncada et al.,
169 1998; Peccerillo et al., 2006; Paonita et al., 2013; Mandarano et al., 2016).
170 The hydrothermal alteration at the surface and of xenoliths ejected during the "Breccia di
171 Commenda" (13th century AD; Gurioli et al., 2012; Di Traglia et al., 2013) and the 1888-90
172 eruptions is characteristic of an acidic hydrothermal system (Fulignati et al., 1998). This is the
173 shallow expression of a deeper intrusive system during its early stage of development (Boyce et al.,
174 2007). The vapor phase is enriched in SO_2, H_2S, HCl, and HF, partly discharging as high-
175 temperature fumaroles; a part also condenses into groundwaters to produce acidic solutions with
176 pH<2 and associated residual silicic alteration. Encrustations of sublimates occur near high-
177 temperature fumaroles, with anomalous Tl, Bi, Te, Pb and As concentrations plus Au grains
178 (Garavelli et al., 1997; Fulignati and Sbrana, 1998; Cheynet et al., 2000). The residual silicic
179 alteration is enveloped by widespread alunite alteration, which is produced by less acidic solutions
180 (Hedenquist and Taran, 2013).
181

4. Results

4.1 Occurrence of magmatic sulfide accessories

In order to assess the presence of magmatic sulfide accessories in the La Fossa recent volcanics, we investigated the dark grey ashes of the lower Palizzi eruptive sequence (Pal A), the pumiceous bombs and lapilli of the two sub-plinian fallout deposits of Palizzi (Pal B and Pal D) and the Upper Pietre Cotte pumiceous bombs and lapilli. The choice of the samples privileged coarse-grained pyroclasts from the fall deposits of the most energetic magmatic eruptions in the recent La Fossa activity, representing rapidly quenched magma parcels, ideal for the study of pre-eruptive conditions of trachytic to rhyolitic magmas. The Pal A ashes, on the other hand, were selected as representative of magmas characterized by a lower degree of differentiation, erupted in the same period.

The juvenile fraction of the Pal A ashes consists of moderately vesicular glass shards with latitic composition (Fig. 3; Table 3) and phenocrysts of plagioclase, clinopyroxene, rare olivine and magnetite. Based on BSE imaging, Pal A ashes did not reveal any sulfides. The Pal B sub-plinian fallout pumice clasts have rhyolitic composition (Fig. 3) and crystals of plagioclase, sanidine and minor clinopyroxene. The Upper Pietre Cotte pumice clasts are nearly aphyric rhyolites with sparsed sanidine microphenocrysts and plagioclase and clinopyroxene crystals (resulting from the mingling with latite magma already described for La Fossa rhyolites, De Astis et al., 2013 and reference therein). In both these rhyolitic products, only rare sulfide globules were found within crystals, and none in the glass. Instead, inspection of the Pal D trachytic pumices revealed that magmatic sulfides are common accessories. In the following, the results of the petrographic and microanalytical study of sulfide and silicate melt inclusions of Pal D trachytic pumice is reported.

4.2 Petrography, bulk and mineral chemistry of the Palizzi trachytic fallout

208

209 The products of the Pal D sub-Plinian fallout show the highest potassium content among the
210 Vulcano rocks (Fig. 3a) and plot in the trachyte field (bulk rock analysis) in the TAS diagram (Total
211 Alkali vs. Silica, inset in Fig. 3a). The bulk rock data cover a small range of SiO_2 (56-61 wt%) with
212 a significant variation in K_2O (5.6-7.5 wt%) and MgO (2.5-1.2 wt%) (Fig. 3b). The phenocryst
213 assemblage, in order of abundance, is plagioclase ($An_{42}Or_6$-$An_{37}Or_9$), clinopyroxene ($Wo_{46}Fs_{12}$-
214 $Wo_{43}Fs_{16}$ with Mg# in the range 71-76), sanidine (An_4Or_{59}-An_3Or_{66}), olivine ($Fo_{64\text{-}66}$) (Fig. 4a),
215 biotite (Mg/(Mg+Fe) = 0.65-0.67) and Ti-magnetite; apatite is a frequent accessory (Fig. 4b). The
216 phenocrysts are in equilibrium with the glassy groundmass, showing the same mineral phases as
217 rare microlites. Calculations of the Mg_v of the melt in equilibrium with clinopyroxene and olivine,
218 using the relation of Wood and Blundy (1997) (Mg_v 34-44), provides values similar to the bulk rock
219 (Mg_v 30-39).

220

221 *4.3 Sulfide globules*

222

223 In the Pal D trachytic pumices, over 60 sulfide globules were found and examined by means of BSE
224 (back-scattered electrons) images. Sulfide globules occur within clinopyroxene, magnetite, olivine,
225 biotite and plagioclase phenocrysts as well as in the glassy groundmass. Sulfides are homogenously
226 distributed in the fallout deposit, from the base to the top. The sulfides within crystals are ovoid and
227 in some cases elongated, suggesting that they were deformed by crystal growth (Fig. 5a, b, c). By
228 contrast, sulfide globules in pumice glass are spherical (Fig. 5d, e). In some cases, the sectioned
229 sulfide shows some glass lining the inclusion walls (Fig. 5f). The sulfides, both in the crystals and
230 in the groundmass glass, are mostly homogeneous when observed with BSE imaging at high
231 magnification. However, in a few cases, some bright spots too small to be analyzed could
232 correspond to unmixed copper/other metal sulfides.

233 The composition of sulfide globules corresponds to pyrrhotite ($Fe_{0.87\text{-}0.95}$ $S_{1.13\text{-}1.05}$, Table 2).

234 Significant Cu contents, up to 2.6 wt.%, and minor concentrations of Co, Ni, Mn and Zn
235 (Co+Mn+Ni+Zn is 0.2-0.5 wt%) are indicated by microanalytical WDS data (Fig. 6; Table 2). The
236 composition of Pal D pyrrhotite is rather homogeneous and the small chemical range does not show
237 any relationship with the type of mineral/glass host (Fig. 6); the only sulfide analyzed in Pal B
238 rhyolite differs from Pal D trachyte sulfides for the pyrrhotite recalculated composition, the closest
239 to the stoichiometric formula FeS ($Fe_{0.97}S_{1.03}$), and for the lower Cu content (Table 2).
240 Most sulfides, both within crystals and in the groundmass glass, do not show any sign of dissolution
241 or resorption. In some cases near cracks, the globules are partially (Fig. 5g) or totally (Fig. 5h)
242 substituted by Fe+Si with a colloform texture, indicating the breakdown and sulfur loss of sulfide.
243
244 *4.4 Water and sulfur content of melt inclusions*
245
246 Melt inclusions are common in phenocrysts of Pal D pumice. They are, in most cases, glassy with
247 lobate shape, without apparent evidence of post-entrapment crystallization (Fig. 4a, b). Hourglass
248 inclusions (i.e. likely in contact with external melt at the time of quenching) are common. The
249 major and trace element compositions of melt inclusions are similar to those of bulk rock (Fig. 3
250 and Table 3). Dissolved sulfur ranges from 156 to 376 ppm, except in one case (68 ppm), and
251 chlorine is between 3300 and 4300 ppm (only one sample shows lower Cl content, 2254 ppm, and
252 one shows higher Cl, 5200 ppm, Table 3). The dissolved H_2O content in MI ranges from 1.01 to
253 2.52 wt% (Table 4), in general agreement with the microprobe totals (Table 3) and does not show a
254 clear trend with sulfur and chlorine content (Fig. 7).
255 In general, higher water contents were measured in melt inclusions hosted in biotite and pyroxene,
256 whereas comparatively lower water contents were obtained from inclusions hosted in olivine.
257 Moreover, values <1 wt% were measured both in hourglass inclusions and glass matrix.
258
259 **5. Discussion**

260

261 *5.1 Pre-eruptive crystallization conditions of the Pal D trachytic magma*

262

263 Mineral and melt inclusions compositions allow the crystallization conditions of the Pal D trachyte
264 in the magma chamber, prior to the eruption, to be estimated.
265 A crystallization temperature in the range of 927-938 °C was obtained using the Ti-in-phlogopite
266 geothermometer (Righter and Carmichael, 1996; the calibration error is ± 50 °C) and biotite
267 compositions (Table 1). Crystallization temperatures in the range of 959-968 °C were calculated
268 using the plagioclase-liquid thermometer (eq. 24a, Putirka 2008; calibration error ± 36 °C), and
269 temperatures in the range 907-929 °C were obtained using the two feldspars thermometer (eq. 27b,
270 Putirka 2008; calibration error ± 30 °C). The values of P and H_2O considered in the equation were
271 50 MPa and 2 wt%, respectively, while the composition of the liquid in equilibrium with crystals
272 was the mean composition of the Pal D groundmass (Table 3). Results obtained from
273 geothermometry estimates are consistent and suggest that the mineral assemblage formed at
274 equilibrium conditions.
275 Models of volatile element solubility in silicate melts constrain the minimum crystallization
276 pressure. Given the common presence of hourglass inclusions, the lowest H_2O contents measured in
277 melt inclusions can indicate the magmatic degassing path (Anderson, 1991). Considering H_2O
278 contents between 1.8 and 2.5 wt.%, we estimate a minimum water saturation pressure between 30
279 and 54 MPa, calculated using the solubility model VolatileCalc 2.0 (Newman and Lowenstern,
280 2002) at 950°C. The dominant volatile in the analyzed trachyte melt inclusions is H_2O, whereas
281 CO_2 has not been detected in Vulcano melt inclusions, even for mafic compositions (i.e., below 50
282 ppm, the FTIR detection limit), indicating it was lost at depth (Clocchiatti et al., 1994b; Fusillo et
283 al., 2015). If there is 50 ppm CO_2 dissolved, the estimated pressure increases about 9 MPa (i.e.,
284 fluid saturation pressure between 39 and 63 MPa). The calculated pressure range is consistent with
285 the shallow portion of the plumbing system envisaged for La Fossa volcano based on melt and fluid

286 inclusion, geophysical and gas geochemistry evidence (Gioncada et al., 1998; Peccerillo et al.,
287 2006; Paonita et al., 2013). The crystallization depth can be constrained on the basis of the
288 calculated minimum water saturation pressure in the range 30-54 MPa. The corresponding
289 calculated minimum depth is between 1200 and 2200 m, considering densities of 2.5 g/cm^3 for the
290 lithostatic load.
291 An oxidation state (fO_2) for the Palizzi trachyte of about ΔNNO -1 to -2 (Fig. 8) can be estimated
292 from biotite compositions used as an oxybarometer (Wones and Eugster, 1965), given the average
293 Fe/(Fe+Mg) ratio of 0.34 (Table 1) and an equilibrium temperature of 950°C.
294
295 *5.2 Sulfide melt saturation*
296
297 The sub-Plinian trachytic products recorded by the Pal D sub-unit clearly show melt immiscibility
298 between sulfide and silicate melts. This process, for the first time described at Vulcano, gives new
299 information about sulfur behavior during magmatic evolution at La Fossa and may assist the
300 discussion whether a similar magmatic-hydrothermal system might evolve to one that is fertile and
301 produce porphyry copper mineralization.
302 The occurrence of sulfide blebs within crystals and in the glass matrix indicates that sulfide
303 saturation and exsolution from silicate melt occurred during crystallization in the magma chamber
304 before the eruption. The spherical shape of the sulfide blebs in the glass matrix provides evidence
305 that immiscibility occurred above the sulfide liquidus at relatively low silicate melt viscosity and,
306 afterwards, the melt was quenched to glass with the eruption. During mixing/mingling of two
307 immiscible melts, the surface tension minimization process drives the less abundant melt to adopt a
308 spherical shape (Mandan, 2017). The coexistence of silicate and sulfide melts at the time of
309 trapping is also indicated by the occurrence of a thin silicate glass film on the wall of some sulfide
310 inclusions hosted in minerals (Fig. 5f). The variable sulfide/silicate ratio of these multiphase
311 inclusions reinforces their interpretation as a heterogeneous trapping of coexisting silicate and

312 sulfide melts. The rapid cooling (syn-eruptive quenching at 950°C) prevented unmixing processes.
313 Upon cooling, the sulfide melt crystallized to pyrrhotite (Table 2).
314 The absence of sulfide inclusions in the Pal A products (early Palizzi period), characterized by a
315 latitic composition (Fig. 3; Table 3), suggests that sulfide melt saturation occurred late in the
316 magma evolution, at the stage of trachyte composition, in the relatively shallow reservoir of La
317 Fossa volcano. Late sulfide saturation is a common feature in arc settings (Jenner et al., 2010; Park
318 et al., 2015). Accordingly, Vulcano basaltic melts are undersaturated with respect to the S-bearing
319 condensed phase, despite a high sulfur content (up to ~2400 ppm) (Métrich and Clocchiatti, 1996;
320 Gioncada et al., 1998; Scaillet and Pichavant, 2005). This is due to the relatively high oxidation
321 state of the Vulcano primitive melts (fO_2 ranging between NNO and NNO +1, Fig. 8; Métrich and
322 Clocchiatti, 1996), which stabilizes the more soluble sulfur species (S^{6+}) in the melt (Carroll and
323 Rutherford, 1985; O'Neill and Mavrogenes, 2002; Jugo et al., 2010). The negative correlation
324 between sulfur content and degree of evolution observed in the transition from basalts to latites
325 (Clocchiatti et al., 1994b; Gioncada et al., 1998), confirmed by recent data on melt inclusions of
326 Vulcanello (Fusillo et al., 2015), has been ascribed to a loss of sulfur by degassing to a volatile
327 phase (Fig. 9). This may have occurred in response to the decrease in solubility with changing melt
328 composition and decreasing temperature during crystallization and differentiation of the magmas
329 (Luhr, 1990, Carroll and Webster, 1994). Alternatively, it was controlled by ascent and
330 decompression of an H_2O-rich melt, promoting exsolution of S into the aqueous fluid instead of the
331 formation of an immiscible sulfide liquid (Scaillet and Pichavant, 2005; Spiliaert et al., 2006;
332 Webster and Botcharnikov, 2011). Exsolution of an aqueous fluid is supported by the generally low
333 H_2O contents of melt inclusions of intermediate composition (< 2 wt%) compared to the basaltic
334 ones (Gioncada et al., 1998). Taking into account the model of the Vulcano plumbing system
335 proposed by Peccerillo et al. (2006) and Paonita et al. (2013), degassing should occur from a 3-5 km
336 reservoir below La Fossa, fed by the volatile-rich basaltic magmas ponding at about 20 km depth.
337 The late sulfide melt saturation in the shallow magmatic storage system, highlighted by Pal D

338 trachytes, was induced by the fO_2 value of trachyte magma (ΔNNO -1 to -2, Fig. 8), which is
339 remarkably lower than that of the basalts (NNO and NNO +1). This converted the soluble sulfate
340 (S^{6+}) into less soluble sulfide (S^{2-}). The occurrence of sulfide melt saturation in Pal D trachytes
341 agrees with the calculated activity of liquid FeS (a_{FeS}) and sulfur concentration at sulfide saturation
342 (SCSS) in the melt (Table 5). We calculated a_{FeS} after Mavrogenes and O'Neill (1999) using
343 thermodynamic data reported by O'Neill and Mavrogenes (2002). The f_{O2} was estimated assuming
344 ΔNNO = -1.5 and f_{S2} using pyrrhotite composition (Froese and Gunter 1976). The calculated a_{FeS}
345 values are ~1, confirming that sulfide saturation is reached at this stage (note that the a_{FeS} in the
346 least evolved products of Vulcano are much lower than 1; Table 5). Furthermore, we calculated the
347 SCSS for Palizzi trachyte melt according to Fortin et al. (2015), assuming a H_2O content between
348 1.8 and 2.5 wt.%, temperature of 950°C and pressure in the range 30-54 MPa. The results suggest
349 that SCSS ranges between 200 and 250 ppm, in agreement with the measured sulfur content of the
350 melt inclusions.
351 The triggering of late sulfide melt-silicate melt immiscibility could be achieved through fractional
352 crystallization, decreasing the Fe^{3+}/Fe^{2+} ratio of the melt (i.e., due to a magnetite-bearing mineral
353 assemblage), and cooling along a buffer curve. Assimilation of a (reduced?) crust (De Astis et al.,
354 1997; Del Moro et al., 1998) could, also, have a role in lowering oxygen fugacity (Park et al.,
355 2015), as well as sulfur input from deeper mafic magmas. Instead, the late sulfide exsolution cannot
356 be ascribed to sudden crystallization of magnetite ("magnetite crisis" of Jenner et al., 2010),
357 because, for Vulcano magmas, magnetite is an early crystallization product (trachybasalts, see Fig.
358 3c, d; De Astis et al., 2013). Sulfide saturation may have been approached by the Vulcano magmas
359 also at some evolutionary stage preceding the trachyte. Indeed, a relatively low fO_2 has been
360 proposed for intermediate and evolved Vulcano products to explain their negative Eu anomaly, with
361 Eu^{2+} partitioning into plagioclase (Gioncada et al., 2003). However, the results here suggest that the
362 main event of sulfide melt immiscibility occurred during the trachytic stage of the Palizzi period,
363 with the production of a significant amount of sulfides.

364

365 *5.3 Inferences on magma fertility and the formation of magmatic-hydrothermal ore systems*

366

367 The timing of sulfide saturation with respect to magmatic differentiation, as well as to the
368 exsolution of a fluid phase, is a critical factor affecting the potential for an intrusion to produce
369 porphyry mineralization. In this work, we show evidence for late sulfide saturation with respect to
370 the magmatic differentiation at La Fossa. This allowed the trachytic magma to enrich in chalcophile
371 elements, resulting in a relatively high Cu content of sulfide blebs (sulfide/silicate melt partition
372 coefficients are ~10^3 for Cu; Ripley et al., 2002). The Pal D sulfide globules show copper
373 concentrations up to 2.6 wt % (Table 2). This is lower than the copper concentrations reaching 6.4
374 wt% reported by Nadeau et al. (2010) for sulfide melts found in scoria samples from Merapi
375 volcano, having similar Fe/Cu, Co/Cu and Ni/Cu ratios (Fig. 10). Copper concentration in Pal D
376 sulfide blebs, particularly the Fe/Cu and Co/Cu ratios (Fig. 10), is instead similar to the composition
377 of sulfide inclusions found in ore-related latite magma at Bingham Canyon porphyry Cu-Mo-Au
378 deposit (Zhang and Audetat, 2017).
379 Most of the sulfides in the Palizzi pumices, either hosted within phenocrystic minerals or in
380 volcanic glass, are well preserved, suggesting that they did not coexist with an exsolved aqueous
381 fluid able to destabilize the sulfides. Crystallization of the Pal D trachyte in absence of an exsolved
382 aqueous fluid is, also, in agreement with the lack of fluid inclusions trapped within crystals. The
383 few altered sulfides (Fig. 5g, h) can be explained by secondary, post-depositional infiltration of
384 external fluids, causing oxidation of sulfide (weathering); they differ from the spongy Fe-oxides
385 described in Sakurajima 1914-15 eruption, interpreted as pyrrhotite relict after syn-eruptive
386 desulfidation (Matsumoto and Nakamura, 2017). The finding of unaltered globules within glass,
387 unprotected by a crystal host, suggests that destabilization and resorption of the immiscible sulfide
388 phases by exsolved aqueous fluids did not occur in the shallow Palizzi trachytic magma chamber.
389 Therefore, sulfur and metals mostly remained locked within magmatic sulfide blebs, in contrast to

other active volcanic systems (Nadeau et al., 2010; Matsumoto and Nakamura, 2017; Edmonds and Mather, 2017).

By contrast, with fractional crystallization to more silicic compositions, chlorine in the silicate melt will increase, since it is only in part sequestered by halogen-bearing minerals such as biotite and apatite. Accordingly, chlorine concentrations up to 5000 ppm were measured in the La Fossa rhyolitic glasses (Gioncada et al., 1998). These high values are sufficient to allow the exsolution of a hydrosaline fluid (Webster, 2004), since they correspond to the chlorine solubility of the La Fossa rhyolite (around 5000 ppm, Table 5), calculated according to Webster et al. (2015), assuming 30-54 MPa and a temperature of 750-850°C, reasonable for rhyolitic magmas similar to La Fossa. The resulting magmatic aqueous fluid phase will be metal-enriched both because of the high aqueous fluid/silicate melt partition coefficients of most base and precious metals ($K_{fluid/melt}$ ~10^1 to 10^2, Pokrovski et al., 2013), and due to sulfide blebs resorption.

In this framework, we must take into account that the Pal-D trachyte magma batch represents a snapshot of the evolution of a magma-hydrothermal system, immediately before its disruption by a sub-Plinian eruption. We argue that during non-eruptive periods, the sulfur and metals locked in the magmatic sulfides at the trachytic stage could have sufficient time to be transferred to an ore-forming fluid, through destabilization and dissolution of the sulfides themselves by exsolving volatiles (Nadeau et al., 2010; Wilkinson, 2013; Fontboté et al., 2017; Edmonds and Mather, 2017). These features suggest that the La Fossa magmas and magmatic-hydrothermal system may be fertile for the genesis of future porphyry-style mineralization, thus representing an active analogue for the study of mineralizing processes in this environment.

6. Conclusions

This study provides evidence for sulfide melt-silicate melt immiscibility at La Fossa volcano. We assess the petrological conditions for the separation of a significant amount of magmatic sulfides in

416 the shallow La Fossa reservoir and discuss the implications for the magmatic-hydrothermal system
417 evolution.
418 The unmixing process took place during the crystallization of the trachytic magma that fed the Pal
419 D sub-Plinian eruption, at a temperature around 950 °C and a minimum pressure of 30-54 MPa
420 (1200-2200 m minimum depth). The dissolved volatile content was 1.8-2.5 wt% of H_2O, 160-380
421 ppm of S and 3300-4300 ppm of Cl. The exsolved sulfide blebs, trapped within minerals and in the
422 groundmass glass, were quenched to pyrrhotite upon eruption.
423 Sulfide melt saturation occurred late with respect to magma differentiation, at the stage of trachytic
424 composition, having a fO_2 value of ΔNNO -1 to -2, lower than that of the oxidized basalts feeding
425 the volcano (between NNO and NNO +1). Copper, as a chalcophile metal, has a high affinity for
426 sulfide melts. The late sulfide saturation of Pal D trachytes implies that the magma became enriched
427 in Cu. This is indicated by the relatively high Cu concentration in the analyzed sulfide blebs, which
428 is comparable to the compositions of sulfides found in ore-related magmas associated with
429 porphyry copper mineralization.
430 The crystallization of the Pal-D trachyte occurred in absence of an exsolved aqueous fluid phase.
431 However, with fractional crystallization towards more silicic compositions (rhyolites), the
432 exsolution of a hydrosaline fluid phase may eventually occur, possibly generating a potentially
433 mineralizing fluids. Furthermore, during quiescent periods, the exsolved aqueous fluids could be
434 enriched by scavenging metals of magmatic sulfides after destabilization and dissolution of the
435 sulfides.
436 Therefore, we suggest that the active magmatic-hydrothermal system of La Fossa may be a
437 potentially fertile environment for the genesis of porphyry-style mineralization and thus represent
438 an active analogue for the study of mineralizing processes at the magma to hydrothermal transition.
439 Future detailed characterization of trace elements (particularly Au) in sulfide globules and in whole
440 rocks may provide further constraints for this idea.
441

Acknowledgements

The authors thank F. Colarieti (Univ. of Pisa), M. Serracino (CNR, Rome), R Ishak (Univ. of Pisa), E. Braschi (Univ. of Florence) for assistance during analytical work. The authors are grateful to the constructive suggestions and criticisms of J. Hedenquist and to the comments of an anonymous reviewer, which helped to improve the quality of the manuscript. Thanks are also due to A. Aiuppa for editorial handling. The research was funded by University of Pisa "Fondi d'Ateneo" (MIUR) to AG, by DPC-INGV project "V3 - Multi-disciplinary analysis of the relationships between tectonic structures and volcanic activity", coordinated by R. Azzaro (INGV-CT), R. De Rosa (Università della Calabria), and by a Tuscany Regional "Pegaso" PhD grant to SC.

Appendix 1: Sampling and analytical methods

The dark grey ashes of the initial phase of the Palizzi eruptive period (Pal A; sampling site TR17 in Figure 1a) were mounted in resin and polished. Pumice clasts of lapilli size from the Pal B rhyolitic fallout deposit (sampling site S134 in Figure 1a), Pal D trachytic fallout deposit (Fig. 2b; sampling site S33 in Figure 1a, at the base, intermediate and upper portions of the outcrop) and Upper Pietre Cotte rhyolitic pumices (Fig. 2d; sampling site S49 in Figure 1a) were gently crushed. Crystals were picked under a stereomicroscope and embedded in resin with their glass coating and additional pumice glass fragments. Polished mounts were studied under a reflected light petrographic microscope.

After carbon-coating, scanning electron microscopy (SEM) and energy-dispersion spectroscopy (EDS) microanalysis were carried out to obtain back-scattered electrons (BSE) images and elemental composition of the sulfides by means of a Philips XL30 equipped with a Dx4i

468 microanalytical device (20 kV filament voltage, 10 mm working distance, up to 5,000X
469 magnification) and a Quanta 450 FE-SEM in the University of Pisa laboratories (20 kV filament
470 voltage, up to 16,000X magnification). Electron probe microanalysis (EPMA) was performed on
471 mineral and glass components with a JEOL JXA-8600 at Consiglio Nazionale delle Ricerche in
472 Florence and a CAMECA SX50 at Consiglio Nazionale delle Ricerche in Rome (15 kV accelerating
473 voltage, 5nA beam current; 10 micron-diameter beam was used for feldspars and glasses to
474 minimize alkali loss).

475 In order to measure the water dissolved in melt inclusions, Raman spectra were acquired
476 using a Thermo Scientific^{TM} DXR^{TM}xi Raman Imaging Microscope at the University of Bristol
477 (UK), School of Earth Sciences. The instrument is equipped with three different lasers i) 455 nm
478 diode, ii) 532 nm doubled Nd:YVO4 DPSS and iii) 633 nm HeNe.

479 Spectra of 40 melt inclusions were acquired between 100 cm^{-1} and 4000 cm^{-1} using a 100x
480 objective, 25 μm confocal pinhole, and a laser power of 3 mW to avoid the sample oxidation (Di
481 Genova et al., 2017). A green laser, which is coupled with 900 lines * mm^{-1} grating, was used to
482 collect the spectra at ~6 micron depth where the Raman signal was found to be maximised. The
483 signal was acquired in 8 s * 10 repetitions. Spectra were corrected for temperature and excitation
484 line effects according to Long (1977). A cubic spline was fit through intervals devoid of peaks in
485 the silicate and water region to subtract the spectra background (Di Genova et al. (2016).
486 Afterwards, the silicate and water band areas were calculated, and the internal calibration reported
487 in Di Genova et al. (2017), using trachytic standards (AMS) from Di Genova et al. (2014), was used
488 to retrieve the amount of dissolved water in each melt inclusion.

489

490

491 **References**

492 Anderson, A.T., 1991. Hourglass inclusions: Theory and application to the Bishop rhyolitic tuff,
493 Am. Mineral. 76, 530-547.

494 Barberi, F., Gasparini, P., Innocenti, F., Villari, L., 1973. Volcanism of the Southern Tyrrhenian
495 Sea and its geodynamic implications. J. Geophys. Res. 78, 5221-5232.

496 Biass, S., Bonadonna, C., Di Traglia, F., Pistolesi, M., Rosi, M., Lestuzzi, P., 2016. Probabilistic
497 evaluation of the physical impact of future tephra fallout events for the Island of Vulcano,
498 Italy. Bull. Volcanol. 1–22.

499 Bolognesi, L., D'Amore, F., 1993. Isotopic variation of the hydrothermal system on Vulcano Island,
500 Italy. Geochim. Cosmochim. Acta 57, 2069-2082.

501 Boyce, A.J., Fulignati, P., Sbrana, A., Fallick, A.E., 2007. Fluids in early stage hydrothermal
502 alteration of high-sulfidation epithermal systems: A view from the Vulcano active
503 hydrothermal system (Aeolian Island, Italy). J. Volcanol. Geotherm. Res. 166, 76-90.

504 Capasso, G., Favara, R., Inguaggiato, S., 1997. Chemical features and isotopic composition of
505 gaseous manifestations on Vulcano Island, Aeolian Islands, Italy: An interpretative model of
506 fluid circulation. Geochim. Cosmochim. Acta 61, 3425-3440.

507 Carroll, M.R., Rutherford, M.J., 1985. Sulfide and sulfate saturation in hydrous silicate melts. J.
508 Geophys. Res. 90, 601-612.

509 Carroll, M.R., Webster, J.D., 1994. Solubilities of sulfur, noble gases, nitrogen, chlorine, and
510 fluorine in magmas. In: M.R. Carroll and J.R. Holloway (eds.), Volatiles in Magmas. Rev.
511 Mineral. 30, 231-279.

512 Cheynet, B., Dall'Aglio, M., Garavelli, A., Grasso, M.F., Vurro, F., 2000. Trace elements from
513 fumaroles at Vulcano Island (Italy): rates of transport and a thermochemical model. J.
514 Volcanol. Geotherm. Res. 95, 273-283.

515 Chiarabba, C., De Gori, P., Speranza, F., 2008. The southern Tyrrhenian subduction zone: Deep
516 geometry, magmatism and Plio-Pleistocene evolution. Earth. Planet. Sci. Lett. 268, 408-423.

517 Chiodini, G., Cioni, R., Marini, L., Panichi, C., 1995. Origin of the fumarolic fluids of Vulcano
518 Island, Italy and implications for volcanic surveillance. Bull. Volcanol. 57, 99-110.

519 Clocchiatti, R., Del Moro, A., Gioncada, A., Joron, J.L., Mosbah, M., Pinarelli, L., Sbrana, A.,
520 1994a. Assessment of a shallow magmatic system: the 1888-1890 eruption, VulcanoIsland,
521 Italy. Bull. Volcanol. 56, 466-486.

522 Clocchiatti, R., Gioncada, A., Mosbah, M., Sbrana, A., 1994b. Possible deep origin of sulfur output
523 at Vulcano (Southern Italy) in the light of melt inclusion studies. Acta Vulcanol. 5, 49-53.

524 Davì, M., De Rosa, R., Barca, D., 2009. A LA-ICP-MS study of minerals in the Rocche Rosse
525 magmatic enclaves: Evidence of a mafic input triggering the latest silicic eruption of Lipari
526 Island (Aeolian Arc, Italy). J. Volcanol. Geotherm. Res. 182, 45–56.

527 De Astis, G., La Volpe, L., Peccerillo, A., Civetta, L., 1997. Volcanological and petrological
528 evolution of the Vulcano Island (Aeolian Arc, Southern Tyrrhenian Sea). J. Geophys. Res.
529 102, 8021-8050.

530 De Astis, G., Peccerillo, A., Kempton, P.D., La Volpe, L., Tsai Wu, W., 2000. Transition from calc-
531 alkaline to potassium-rich magmatism in subduction environments: Geochemical and Sr, Nd,
532 Pb isotopic constraints from the island of Vulcano (Aeolian arc). Contrib. Mineral. Petrol.
533 139, 684-703.

534 De Astis, G., Lucchi, F., Dellino, P., La Volpe, L., Tranne, C.A., Frezzotti,, M.L., Peccerillo, A.,
535 2013. Geology volcanic history and petrology of Vulcano (central Aeolian archipelago). Geol.
536 Soc. Lond. Mem. 37, 281-349.

537 Di Genova, D., Romano, C., Giordano, D., Alletti, M., 2014. Heat capacity, configurational heat
538 capacity and fragility of hydrous magmas. Geochim. Cosmochim. Acta 142, 314–333.

539 Di Genova, D., Kolzenburg, S., Vona, A., Chevrel, M.O.O., Hess, K.-U., Neuville, D.R.R., Ertel-
540 ingrisch, W., Romano, C., Dingwell, D.B.B., 2016. Raman spectra of Martian glass
541 analogues: A tool to approximate their chemical composition. J. Geophys. Res. Planets 121,
542 740–752.

543 Di Genova, D., Sicola, S., Romano, C., Vona, A., Fanara, S., Spina, L., 2017. Effect of iron and
544 nanolites on Raman spectra of volcanic glasses: reassessment of existing strategies to estimate
545 the water content. Chem. Geol. 475, 76–86.

546 Del Moro, A., Gioncada, A., Pinarelli, L., Sbrana, A., Joron, J.L., 1998. Sr, Nd, Pb isotope evidence
547 for open system evolution at Vulcano, Aeolian Arc, Italy. Lithos 43, 81-106.

548 Di Traglia, F., Pistolesi, M., Rosi, M., Bonadonna, C., Fusillo, R., and Roverato, M., 2013. Growth
549 and erosion: The volcanic geology and morphological evolution of La Fossa (Island of
550 Vulcano, Southern Italy) in the last 1000 years. Geomorphology 194, 94–107.

551 Edmonds, M., Mather, T.A., 2017. Volcanic sulfides and outgassing. Elements 13, 105-110.

552 Fontboté, L., Kouzmanov, K., Chiaradia, M., Pokrovski, G.S., 2017. Sulfide minerals in
553 hydrothermal deposits. Elements 13, 97-103.

554 Fortin, M.-A., Riddle, J., Desjardins-Langlais, Y., Baker, D.R., 2015. The effect of water on the
555 sulfur concentration at sulfide saturation (SCSS) in natural melts. Geochim. Cosmochim. Acta
556 160, 100-116.

557 Francalanci, L., Tommasini, S., Conticelli, S., 2004. The volcanic activity of Stromboli in the 1906
558 – 1998 A.D. period: mineralogical, geochemical and isotope data relevant to the
559 understanding of plumbing system. J. Volcanol. Geotherm. Res. 131, 179–211.

560 Frazzetta, G., Gillot, P.Y., La Volpe, L., Sheridan, M.F., 1984. Volcanic hazards of Fossa of
561 Vulcano: data from the last 6,000 years. Bull. Volcanol. 47, 105-124.

562 Froese, E., Gunter, A.E., 1976. A note on the pyrrhotite-sulfur vapor equilibrium. Econ. Geol. 71,
563 1589-1594.

564 Fulignati, P., Sbrana, A., 1998. Presence of native gold and tellurium in the active high-sulfidation
565 hydrothermal system of the La Fossa volcano (Vulcano, Italy). J. Volcanol. Geotherm. Res.
566 86, 187-198.

567 Fulignati, P., Gioncada, A., Sbrana, A., 1998. Geologic model of the magmatic-hydrothermal
568 system of Vulcano (Aeolian Island, Italy). Mineral. Petrol. 62, 195-222.

569 Fusillo, R., Di Traglia, F., Gioncada, A., Pistolesi, M., Wallace, P.J., Rosi, M., 2015. Deciphering
570 post-caldera volcanism: insight into the Vulcanello (Island of Vulcano, Southern Italy)
571 eruptive activity based on geological and petrological constraints. Bull. Volcanol. 77, 76.

572 Garavelli, A., Laviano, R., Vurro, F., 1997. Sublimate deposition from hydrothermal fluids at the
573 Fossa crater-Vulcano, Italy. Eur. J. Mineral. 9, 423-432.

574 Georgatou, A., Chiaradia, M., Rezeau, H., Walle, M., 2018. Magmatic sulphides in Quaternary
575 Ecuadorian arc magmas. Lithos 296-299, 580-599.

576 Gioncada, A., 1997. L'attività eruttiva degli ultimi 50000 anni di Vulcano(Eolie): aspetti
577 vulcanologici e magmatologici. PhD thesis, University of Pisa, Italy, 188 pp. In Italian

578 Gioncada, A., Sbrana, A., 1991. “La Fossa Caldera”, Vulcano: inferences from deep drillings. Acta
579 Vulcanol. 1, 115-126.

580 Gioncada, A., Clocchiatti, R., Sbrana, A., Bottazzi, P., Massare, D., Ottolini, L., 1998. A study of
581 melt inclusions at Vulcano (Aeolian Islands, Italy): insights on the primitive magmas and on
582 the volcanic feeding system. Bull. Volcanol. 60, 286-306.

583 Gioncada, A., Mazzuoli, R., Bisson, M., Pareschi, T., 2003. Petrology of volcanic products younger
584 than 42 ka on the Lipari–Vulcano complex (Aeolian Islands, Italy): an example of volcanism
585 controlled by tectonics. J. Volcanol. Geotherm. Res. 122, 191-220.

586 Gurioli, L., Zanella, E., Gioncada, A., Sbrana, A., 2012. The historic magmatic-hydrothermal
587 eruption of the Breccia di Commenda, Vulcano, Italy. Bull. Volcanol. 74, 1235-1254.

588 Halter, W.E., Heinrich, C.A., Pettke, T., 2005. Magma evolution and the formation of porphyry Cu-
589 Au ore fluids: evidence from silicate and sulfide melt inclusions. Mineral. Deposita 39, 845-
590 863.

591 Hedenquist, J.W., Lowenstern, J.B., 1994. The role of magmas in the formation of hydrothermal
592 ore-deposits. Nature 370, 519-527.

593 Hedenquist, J.W., Taran, Y.A., 2013. Modeling the formation of advanced argillic lithocaps:
594 volcanic vapor condensation above porphyry intrusions. Econ. Geol. 108, 1523-1540.

595 Huebner, J.S., Sato, M., 1970. The oxygen fugacity-temperature relationships of manganese oxide
596 and nickel oxide buffers. Am. Mineral. 55, 934-952.

597 Jenner, F.E., O'Neill, H.S.C., Arculus, R.J., Mavrogenes, J.A., 2010. The magnetite crisis in the
598 evolution of arc-related magmas and the initial concentration of Au, Ag and Cu. J. Petrol. 51,
599 2445-2464.

600 Jugo, P.J., Wilke, M., Botcharnikov, R.E., 2010. Sulfur K-edge XANES analysis of natural and
601 synthetic basaltic glasses: implications for S speciation and S content as function of oxygen
602 fugacity. Geochim. Cosmochim. Acta 74, 5926-5938.

603 Keller, J., 1980. The island of Vulcano. Rend. Soc. It. Miner. Petr. 36, 369-414.

604 Le Voyer, M., Asimow, P.D., Mosenfelder, J.L., Guan, Y., Wallace, P.J., Schiano, P., Stolper,
605 E.M., Eiler, J.M., 2014. Zonation of H_2O and F concentrations around melt inclusions in
606 olivines. J. Petrol. 55, 685-707.

607 Long, D.A., 1977. Raman Spectroscopy. vol. 2. McGraw-Hill, pp. 276.

608 Lowczak, J.N., Campbell, I.H., Cocker, H., Park, J.-W., Cooke, D.R., 2018. Platinum-group
609 element geochemistry of the Forest Reef Volcanics, southeastern Australia: implications for
610 porphyry Au-Cu mineralization. Geochim. Cosmochim. Acta 220, 385-406.

611 Luhr, J.F., 1990. Experimental phase relations of water- and sulfur-saturated arc magmas and the
612 1982 eruptions of El Chichon Volcano. J. Petrol. 31, 1071-1114.

613 Mandan, C.L., 2017. Volatile transport of metals in the andesitic magmatic-hydrothermal system of
614 White Island. PhD thesis, Victoria University of wellington, New Zealand, 209 pp.

615 Mandarano, M., Paonita, A., Martelli, M., Viccaro, M., Nicotra, E., Millar, I.L., 2016. Revealing
616 magma degassing below closed-conduit active volcanoes: geochemical features of volcanic
617 rocks versus fumarolic fluids at Vulcano (Aeolian Islands, Italy). Lithos 248-251, 272-287.

618 Matsumoto, K., Nakamura, M., 2017. Syn-eruptive breakdown of pyrrhotite: a record of magma
619 fragmentation, air entrainment, and oxidation. Contrib. Mineral. Petrol. 172, 83.

620 Mavrogenes, J.A., and O'Neill, H.S.C., 1999. Geochim. Cosmochim. Acta 60, 4151-4160. The
621 relative effects of pressure, temperature and oxygen fugacity on the solubility of sulfide in
622 mafic magmas. Geochim. Cosmochim. Acta 63, 11783-1180.

623 Mazzuoli, R., Tortorici, L., Ventura, G. 1995. Oblique rifting in Salina, Lipari and Vulcano Islands
624 (Aeolian Islands, Southern Italy). Terra Nova 7, 444-452.

625 Metrich, N., Clocchiatti, R., 1996. Sulfur abundance and its speciation in oxidized alkaline melts.
626 Geochim. Cosmochim. Acta 60, 4151-4160.

627 Nadeau, O., Williams-Jones, A.E., Stix, J., 2010. Sulphide magma as a source of metals in arc-
628 related magmatic hydrothermal ore fluids. Nature Geosci. 3, 501-505.

629 Newman, S., Lowenstern, J.B., 2002. VolatileCalc: a silicate melt-H_2O-CO_2 solution model written
630 in Visual Basic for excel. Comp. Geosci. 28, 597-604.

631 O'Neill, H.S.C., Mavrogenes, J.A., 2002. The sulfide capacity and the sulfur content at sulfide
632 saturation of silicate melts at 1400°C and 1 bar. J. Petrol. 43, 1049-1087.

633 Paonita, A., Federico, C., Bonfanti, P., Capasso, G., Inguaggiato, S., Italiano, F., Madonia, P.,
634 Pecoraino, G., Sortino, F., 2013. The episodic and abrupt geochemical changes at La Fossa
635 fumaroles (Vulcano Island, Italy) and related constraints on the dynamics, structure, and
636 compositions of the magmatic system. Geochim. Cosmochim. Acta 120, 158-178.

637 Park, J.-W., Campbell, I.H., Kim, J., Moon, J.-W., 2015. The role of late sulfide saturation in the
638 formation of a Cu- and Au-rich magma: insights from the platinum group element
639 geochemistry of Niuatahi-Motutahi lavas, Tonga rear arc. J. Petrol. 56, 59-81.

640 Peccerillo, A., Frezzotti, M.L., De Astis, G., Ventura, G., 2006. Modeling the magma plumbing
641 system of Vulcano (Aeolian Islands, Italy) by integrated fluid-inclusion geobarometry,
642 petrology, and geophysics. Geology 34, 17-20.

643 Piochi, M., De Astis, G., Petrelli, M., Ventura, G., Sulpizio, R., Zanetti, A., 2009. Constraining the
644 recent plumbing system of Vulcano (Aeolian Arc, Italy) by textural, petrological, and fractal
645 analysis: The 1739 A.D. Pietre Cotte lava flow. Geochem. Geophys. Geosyst. 10,
646 doi:10.1029/2008GC002176.

647 Pokrovski, G.S., Borisova, A.Y., Bychkov, A.Y., 2013. Speciation and transport of metals and
648 metalloids in geological vapors. Rev. Mineral. Geochem. 76, 165-218.

649 Putirka, K.D., 2008. Thermometers and barometers for volcanic systems. Rev. Mineral. Geochem.
650 69, 61-120.

651 Richards, J.P., 2011. Magmatic to hydrothermal metal fluxes in convergent and collided margins.
652 Ore Geol. Rev. 40, 1-26.

653 Richards, J.P., 2015. The oxidation state, and sulfur and Cu contents of arc magmas:implications
654 for metallogeny. Lithos 233, 27-45.

655 Righter, K., Carmichael, I.S., 1996. Phase equilibria of phlogopite lamprophyres from western
656 Mexico: Biotite-liquid equilibria and PT estimates for biotite-bearing igneous rocks. Contrib.
657 Mineral. Petrol. 123, 1-21.

658 Ripley, E.M., Brophy, J.G., Li, C.S., 2002. Copper solubility in a basaltic melt and sulfide/silicate
659 melt partition coefficients of Cu and Fe. Geochim. Cosmochim. Acta 66, 2791-2800.

660 Ruch, J., Vezzoli, L., De Rosa, R., Di Lorenzo, R., Acocella, V., 2016. Magmatic control along a
661 strike-slip volcanic arc: the central Aeolian arc (Italy). Tectonics 35, 407-424.

662 Scaillet, B., Pichavant, M., 2005. A model of sulphur solubility for hydrous mafic melts: application
663 to the determination of magmatic fluid compositions of Italian volcanoes. Annals Geophys.
664 48, 671-698.

665 Sillitoe, R.H., 2010. Porphyry copper systems. Econ. Geol. 105, 3-41.

666 Ventura, G., Vilardo, G., Milano, G., Pino, N.A., 1999. Relationships among crustal structure
667 volcanism and strike-slip tectonics in the Lipari-Vulcano volcanic complex (Aeolian Islands,
668 Southern Tyrrhenian Sea, Italy). Phys. Earth Planet. Inter. 116, 31-52.

669 Webster J.D., 2004. The exsolution of magmatic hydrosaline chloride liquids. Chem. Geol. 210, 33-
670 48.

671 Webster, J.D., Botcharnikov, R.E., 2011. Distribution of sulfur between melt and fluid in S-O-H-C-
672 Cl-bearing magmatic systems at shallow crustal pressures and temperatures. Rev. Mineral.
673 Geochem. 73, 247-283.

674 Webster J.D., Vetere, F., Botcharnikov, R.E., Goldoff, B., McBirney, A., Doherty, A.L., 2015.
675 Experimental and modelled chlorine solubilities in aluminosilicate melts at 1 to 7000 bars and
676 700 to 1250 °C: Applications to magmas of Augustine volcano, Alaska. Am. Mineral. 100,
677 522-535.

678 Wilkinson, J.J., 2013. Triggers for the formation of porphyry ore deposits in magmatic arcs. Nature
679 Geosci. 6, 917-925.

680 Wones, D.R., Eugster, H.P., 1965. Stability of biotite: experiment, theory and application. Am.
681 Mineral. 50, 1228-1272.

682 Wood, B.J., Blundy, J.D., 1997. A predictive model for rare earth element partitioning between
683 pyroxene and anhydrous silicate melt. Contrib. Mineral. Petrol. 129, 166–181.

684 Zelenski, M., Kamenetsky, V.S., Mavrogenes, J.A., Gurenko, A.A., Danyushevsky, L.V., 2017.
685 Silicate-sulfide liquid immiscibility in modern arc basalt (Tolbachik volcano, Kamchatka):
686 Part I. Occurrence and compositions of sulfide melts. Chem. Geol. 478, 102-111.

687 Zhang, D., Audetat, A., 2017. What caused the formation of the giant Bingham Canyon porphyry
688 Cu-Mo-Au deposit? Insights from melt inclusions and magmatic sulfides. Econ. Geol. 112,
689 221-244.

690

691 **Figure captions**

692

693 **Fig. 1.** a) Map (overlaying an orthophoto and a shaded relief topographic map) of the Island of
694 Vulcano, highlighting the main volcanological features. The sampling sites of this study are also
695 reported. In the insert, the location of the Island of Vulcano within the Aeolian Archipelago is
696 shown. b) Synthetic log of the deposits related to the last 1000 years of eruptive activity at the La
697 Fossa cone, modified after Piochi et al. (2009) and Di Traglia et al. (2013).

Fig. 2. Features of the volcaniclastic deposits analysed in this work. a) Pal B rhyolitic sub-plinian fallout layer (Di Traglia et al., 2013) at the sampling site S134; b) the entire volcaniclastic sequence associated with the Palizzi Eruptive Unit, outcropping in a ravine located downslope with respect the sampling site S77; c) Pal B trachytic sub-plinian fallout layer (Di Traglia et al., 2013) at the sampling site S33; d) the entire volcaniclastic sequence associated with the Upper Pietre Cotte, Post-1739 and 1888-1890 eruptive deposits.

Fig. 3. Selected major (a, b, c) and trace (d) elements variation diagrams vs SiO_2 (wt%) for Pal D pumice (Gioncada,1997) and melt inclusions and Pal D and Pal A groundmass glass (this work). Total alkali vs SiO_2 (TAS) as an inset in a. Major elements are recalculated to 100 on anhydrous basis to allow comparison of melt inclusions and whole rock. Other whole rock data, with highlighted Pal B, Pal C and Pal F samples, are from Clocchiatti et al. (1994a), Gioncada (1997), Del Moro et al. (1998), De Astis et al. (2013), Davì et al. (2009), Fusillo et al. (2015); melt inclusions data for La Sommata are from Gioncada et al. (1998) and Le Voyer et al. (2014).

Fig. 4. Transmitted light microphotos of olivine (a) and clinopyroxene (b) crystals of the Palizzi Pal D pumices. Examples of glassy melt inclusions (MI) and of sulfide globules trapped with accessories (apatite) are shown.

Fig. 5. Magmatic sulfides in the Palizzi Pal D pumice: (a, b) the same sulfides under reflected light (a) and BSEI, back-scattered electron imaging (b); the sulfide on the left shows a slightly heterogeneous appearance; (c) sulfide in clinopyroxene; (d) sulfides trapped within olivine and in the pumice glass; (e) close-up of the sulfide in pumice glass in d; (f) sulfide trapped with silicate glass; (g, h) examples of partially (g) and totally (h) altered sulfides.

Fig. 6. Ternary graph in the Fe-Cu-S system showing the composition and the mineral/glass host of the sulfide bleb analyzed in Pal D trachyte and Pal B rhyolite sub-units of the Palizzi eruptive sequence. Fe, Cu and S are in wt.%.

Fig. 7. H_2O vs Cl and H_2O vs S diagrams for the melt inclusions of Pal D trachytes (data in Table 3).

724 **Fig. 8.** Log oxygen fugacity vs. temperature, showing the fO_2 values of La Sommata basalts (from
725 Metrich and Clocchiatti, 1996) and Palizzi trachytes (calculated in this work). Ni-NiO buffer
726 (Huebner and Sato, 1970) is plotted for comparison.
727 **Fig. 9.** Range of sulfur content in Pal D trachyte melt inclusions (this work) with the calculated
728 sulfur concentration at sulfide saturation (SCSS), compared to the sulfur content measured in melt
729 inclusions of Vulcanello shoshonites and latites (black boxes, Fusillo et al., 2015) and to the entire
730 variation of sulfur content with respect to the degree of evolution at Vulcano (white boxes,
731 Gioncada et al., 1998). B = basalt; TB = trachybasalt; SH = shoshonite; LT = latite; TR = Pal D
732 trachyte; RY = rhyolite.
733 **Fig. 10**. Fe/Cu-Co/Cu-Ni/Cu ratios. Plots of the Cu (ppm) concentration vs. Fe (ppm), Co (ppm)
734 and Ni (ppm) concentrations of sulfide blebs in Palizzi trachytes. Straight lines representative of
735 various Fe/Cu, Co/Cu and Ni/Cu ratios are also shown for comparison. The gray fields represent the
736 composition of sulfide inclusions at Merapi volcano, from data of Nadeau et al. (2010). The ruled
737 fields represent the composition of sulfide inclusions in ore-related latite magma at Bingham
738 Canyon porphyry Cu-Mo-Au deposit, from data of Zhang and Audetat (2017).
739

741 **Table captions**

742 Table 1. Representative (EPMA, wt%) analyses of phenocrysts of olivine (ol), clinopyroxene (cpx),
743 plagioclase (pl), sanidine (sa) and biotite (bt) from Pal D trachyte. Major elements (EPMA)
744 expressed as wt %. bdl: below detection limit.

745 Table 2. Electron microprobe analyses (wt %) of sulfide globules in the Pal D (trachyte) and Pal B
746 (rhyolite) material. Two and, in one case, three analyses were carried out on large sulfides to check
747 for homogeneity, and mean [n] and standard deviation (SD) are reported. bdl: below detection limit.
748 bt: biotite; cpx: clinopyroxene; ol: olivine, pl: plagioclase; sa: sanidine; glomer: glomerophyre. Po
749 formula: pyrrhotite chemical formula calculated from microprobe analysis of mineral major
750 elements.

751 Table 3. Major element (wt.%), S, Cl and water content of melt inclusion (MI) of the Pal D pumice.
752 Major elements, chlorine and sulfur by electron microprobe; water content by Raman spectroscopy
753 (see Table 4 for the complete water content dataset). Mean and standard deviation (SD) of major
754 element analyses of the glassy groundmass of Pal A and Pal D products are also reported; bdl:
755 below detection limit; nd: not determined; bt: biotite; cpx: clinopyroxene, ol: olivine, pl:
756 plagioclase.

757 Table 4. Raman spectroscopy determination of H2O content of melt inclusions (MI) and matrix
758 glass of Pal D pumices; bt: biotite; cpx: clinopyroxene; ol: olivine, pl: plagioclase.

759 Table 5. Compositional data (MgO wt% and dissolved S in melt inclusions) and summary of the
760 parameters for Pal D trachytic magma measured or calculated in this work (see text for
761 explanation), for La Sommata basalt and for La Fossa rhyolite. MI: melt inclusions; SCSS: sulfur
762 concentration at sulfide saturation.

763

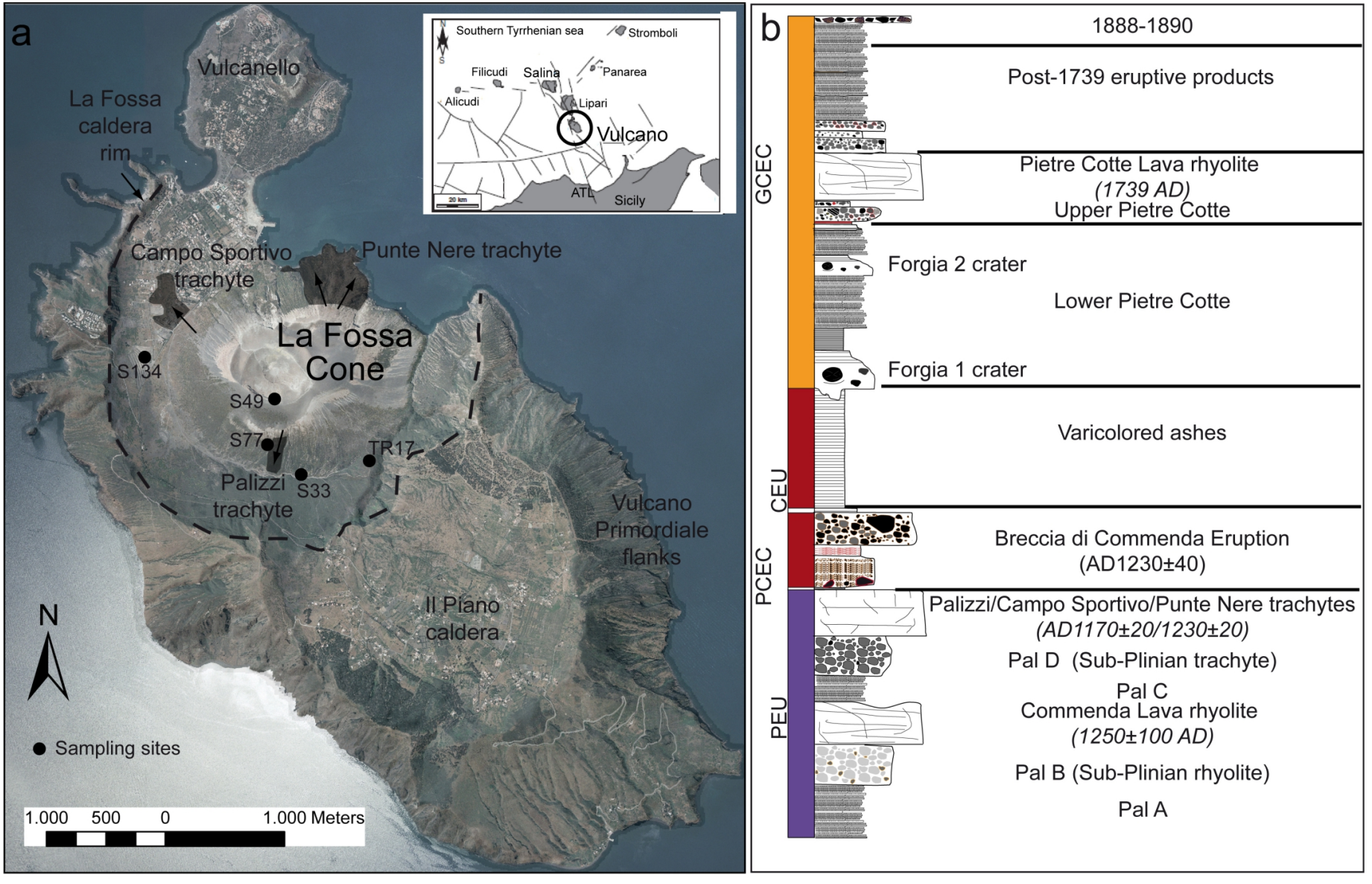
a
Vulcanello
La Fossa caldera rim
Campo Sportivo trachyte
Punte Nere trachyte
La Fossa Cone
S134
S49
S77
TR17
Palizzi trachyte
S33
Vulcano Primordiale flanks
Il Piano caldera
N
Sampling sites
1.000 500 0 1.000 Meters
Southern Tyrrhenian sea
Stromboli
Filicudi
Salina
Panarea
Alicudi
Lipari
Vulcano
ATL
Sicily
b
1888-1890
Post-1739 eruptive products
Pietre Cotte Lava rhyolite
(1739 AD)
Upper Pietre Cotte
Forgia 2 crater
Lower Pietre Cotte
Forgia 1 crater
Varicolored ashes
Breccia di Commenda Eruption
(AD1230±40)
Palizzi/Campo Sportivo/Punte Nere trachytes
(AD1170±20/1230±20)
Pal D (Sub-Plinian trachyte)
Pal C
Commenda Lava rhyolite
(1250±100 AD)
Pal B (Sub-Plinian rhyolite)
Pal A
GCEC
CEU
PCEC
PEU

Figure 1

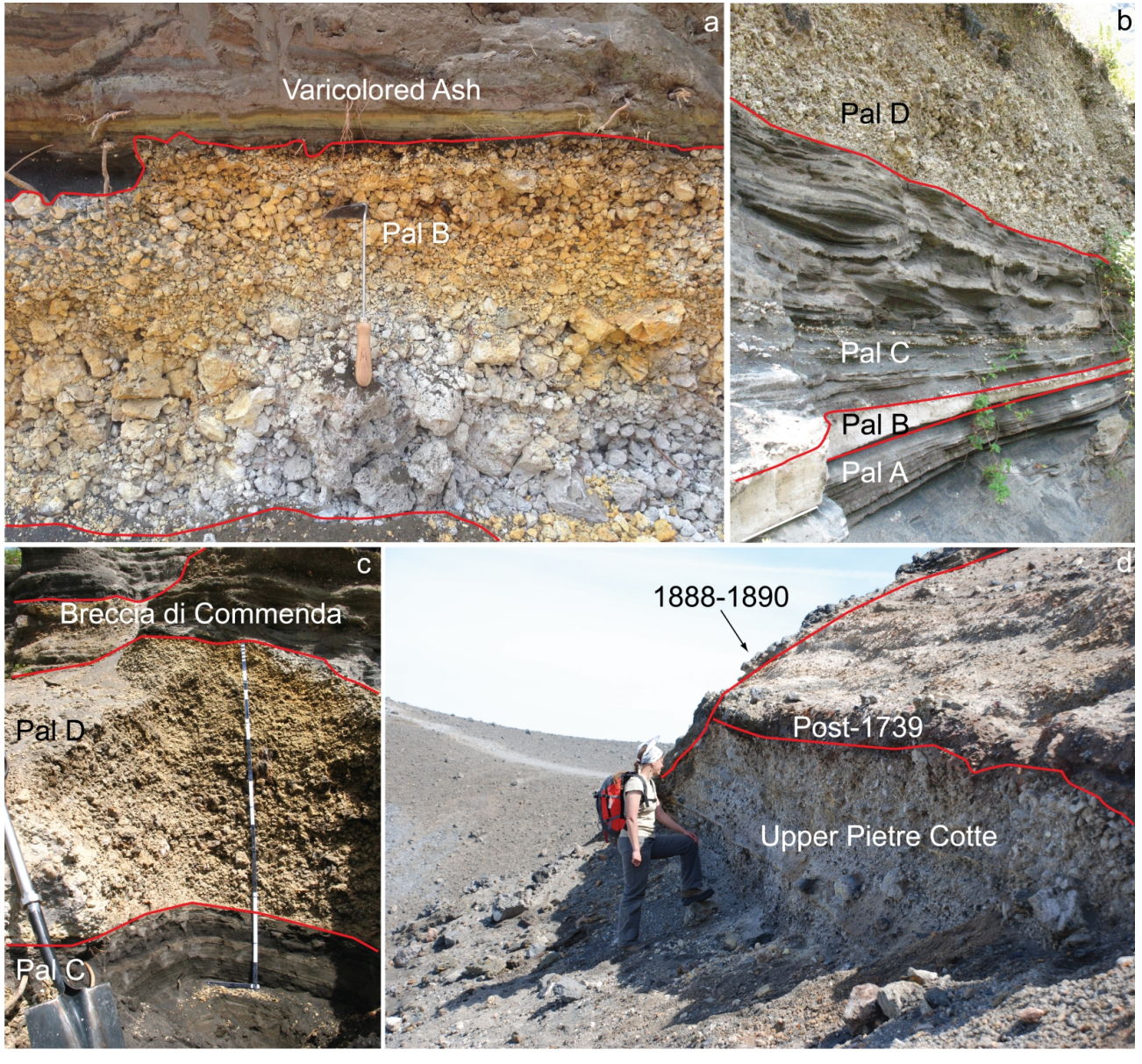
a
Varicolored Ash
Pal B
b
Pal D
Pal C
Pal B
Pal A
c
Breccia di Commenda
Pal D
Pal C
d
1888-1890
Post-1739
Upper Pietre Cotte

Figure 2

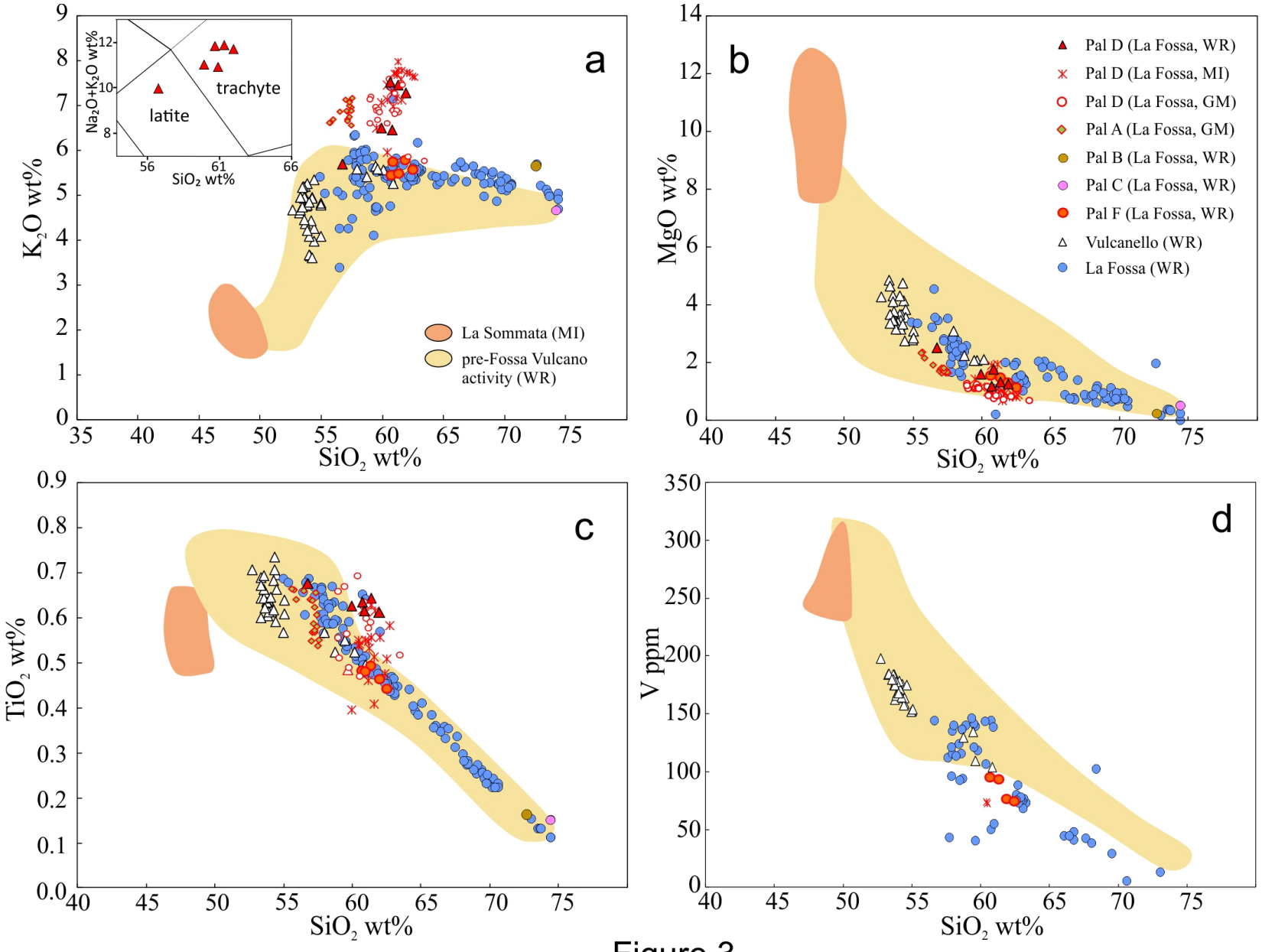
a
b
c
d
K_2O wt%
SiO_2 wt%
Na_2O+K_2O wt%
trachyte
latite
La Sommata (MI)
pre-Fossa Vulcano activity (WR)
MgO wt%
Pal D (La Fossa, WR)
Pal D (La Fossa, MI)
Pal D (La Fossa, GM)
Pal A (La Fossa, GM)
Pal B (La Fossa, WR)
Pal C (La Fossa, WR)
Pal F (La Fossa, WR)
Vulcanello (WR)
La Fossa (WR)
TiO_2 wt%
V ppm

Figure 3

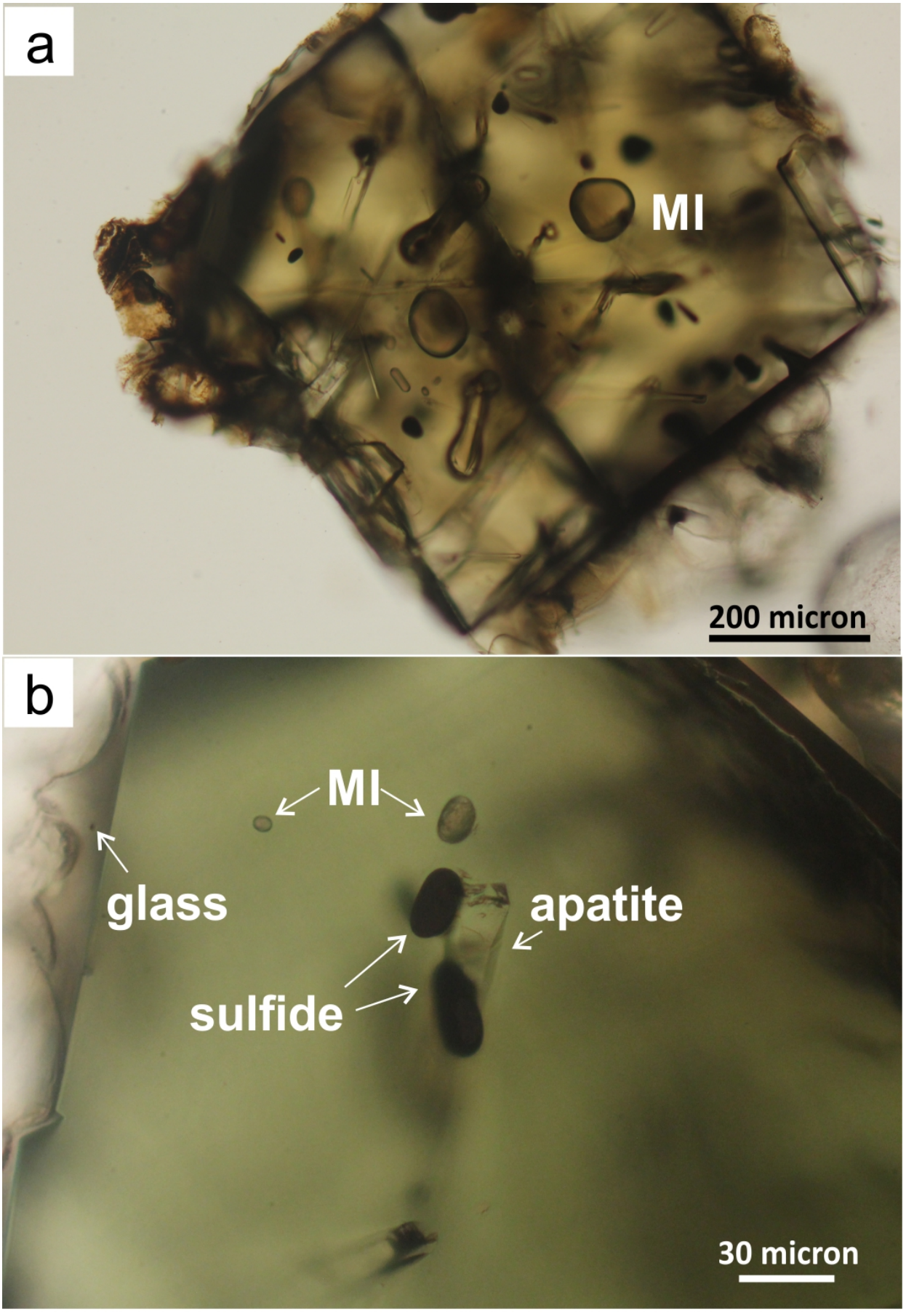

Figure 4

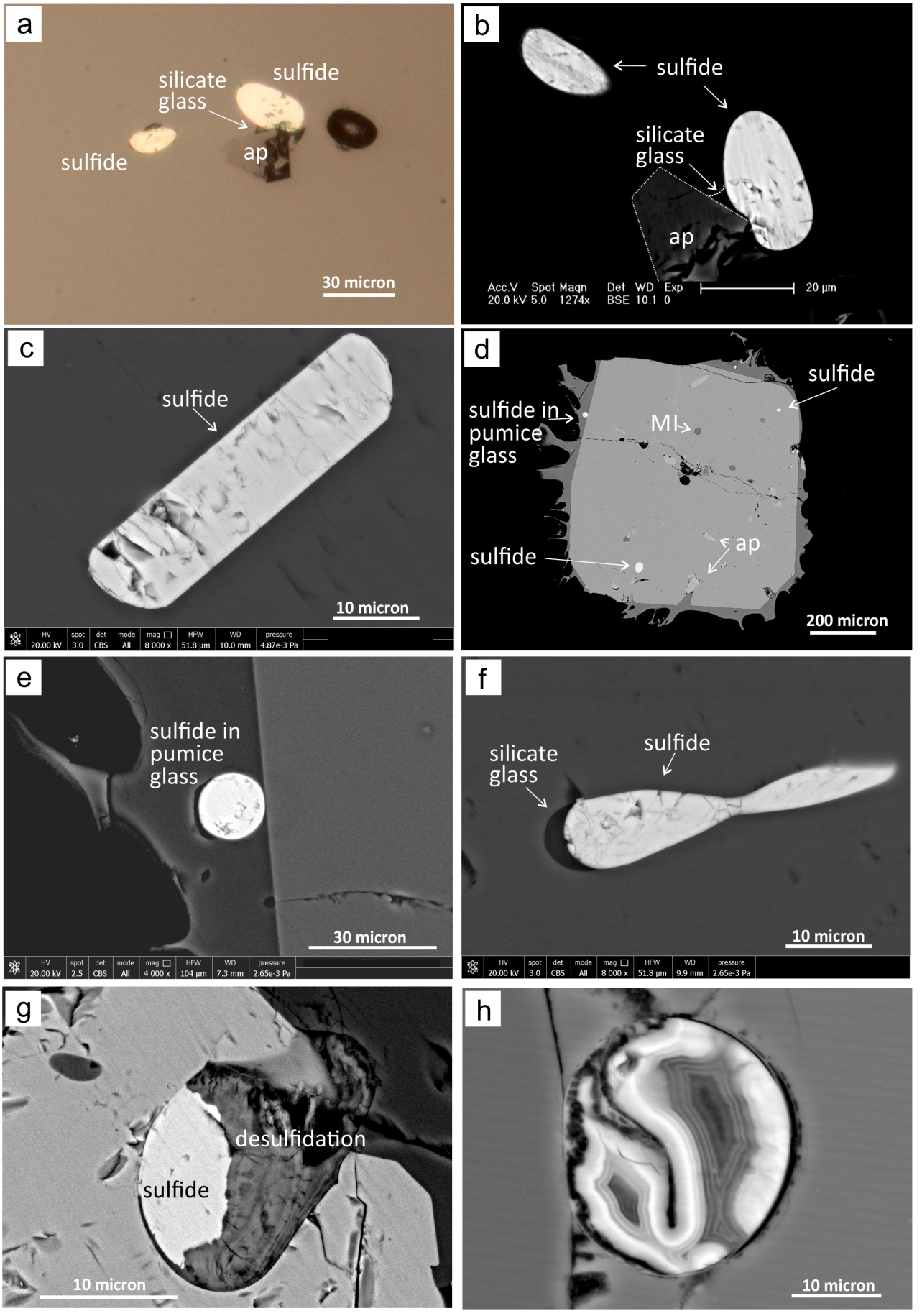
a
silicate glass
sulfide
sulfide
ap
30 micron
b
sulfide
silicate glass
ap
Acc.V Spot Magn Det WD Exp
20.0 kV 5.0 1274x BSE 10.1 0
20 µm
c
sulfide
10 micron
HV spot det mode mag HFW WD pressure
20.00 kV 3.0 CBS All 8 000 x 51.8 µm 10.0 mm 4.87e-3 Pa
d
sulfide
sulfide in pumice glass
MI
ap
sulfide
200 micron
e
sulfide in pumice glass
30 micron
HV spot det mode mag HFW WD pressure
20.00 kV 2.5 CBS All 4 000 x 104 µm 7.3 mm 2.65e-3 Pa
f
silicate glass
sulfide
10 micron
HV spot det mode mag HFW WD pressure
20.00 kV 3.0 CBS All 8 000 x 51.8 µm 9.9 mm 2.65e-3 Pa
g
desulfidation
sulfide
10 micron
h
10 micron

Figure 5

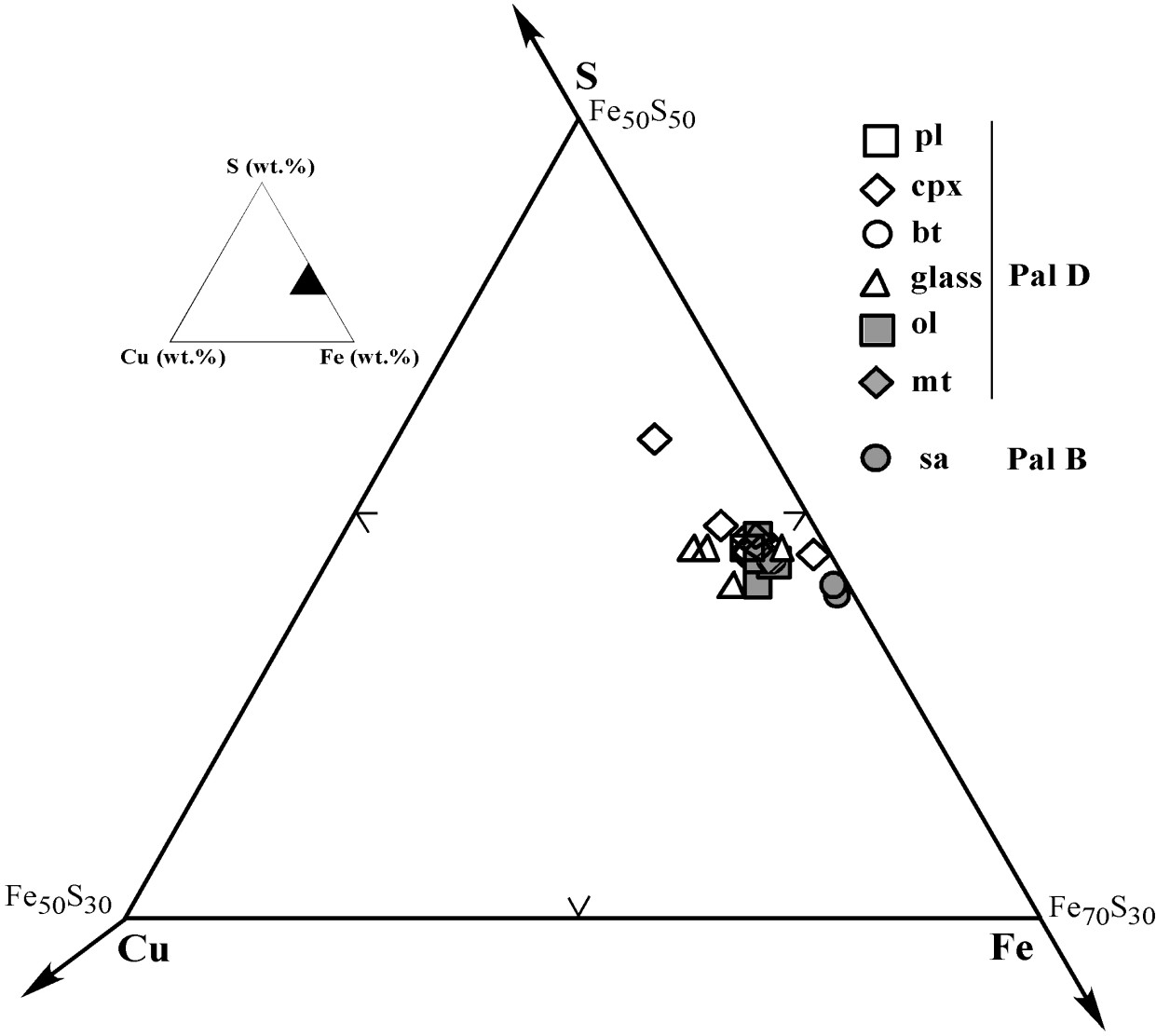
S
Fe50S50
S (wt.%)
Cu (wt.%)
Fe (wt.%)
pl
cpx
bt
glass
ol
mt
Pal D
sa
Pal B
Fe50S30
Fe70S30
Cu
Fe

Figure 6

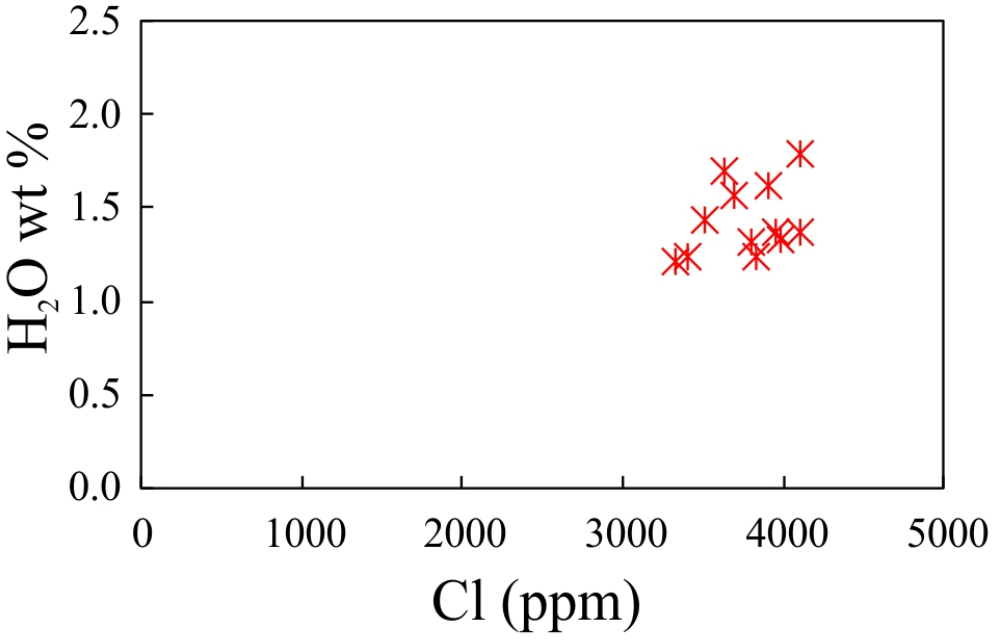
2.5
2.0
1.5
1.0
0.5
0.0
H2O wt %
0
1000
2000
3000
4000
5000
Cl (ppm)

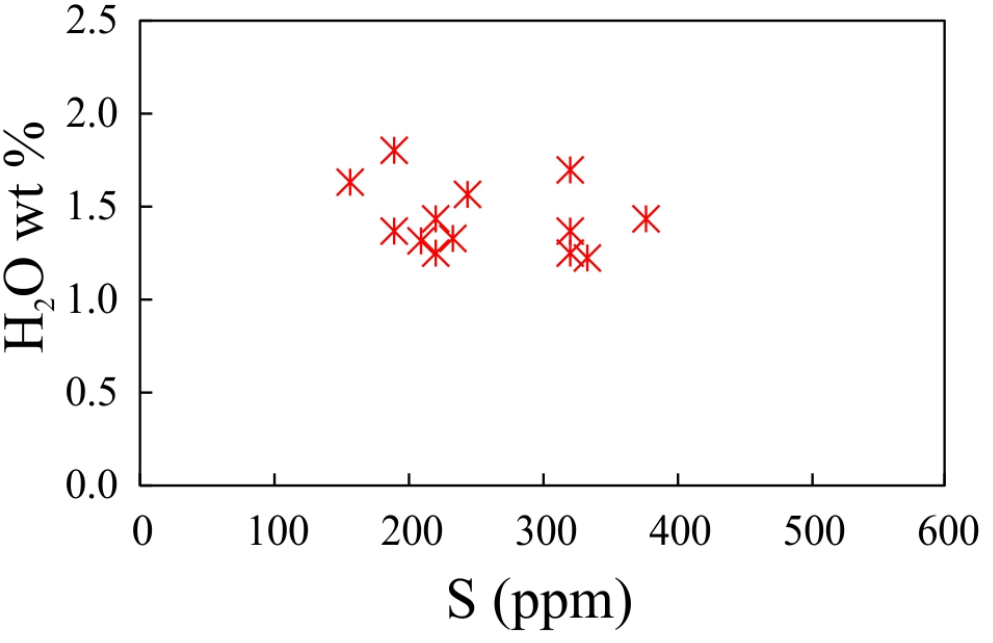
2.5
2.0
1.5
1.0
0.5
0.0
H2O wt %
0
100
200
300
400
500
600
S (ppm)

Figure 7

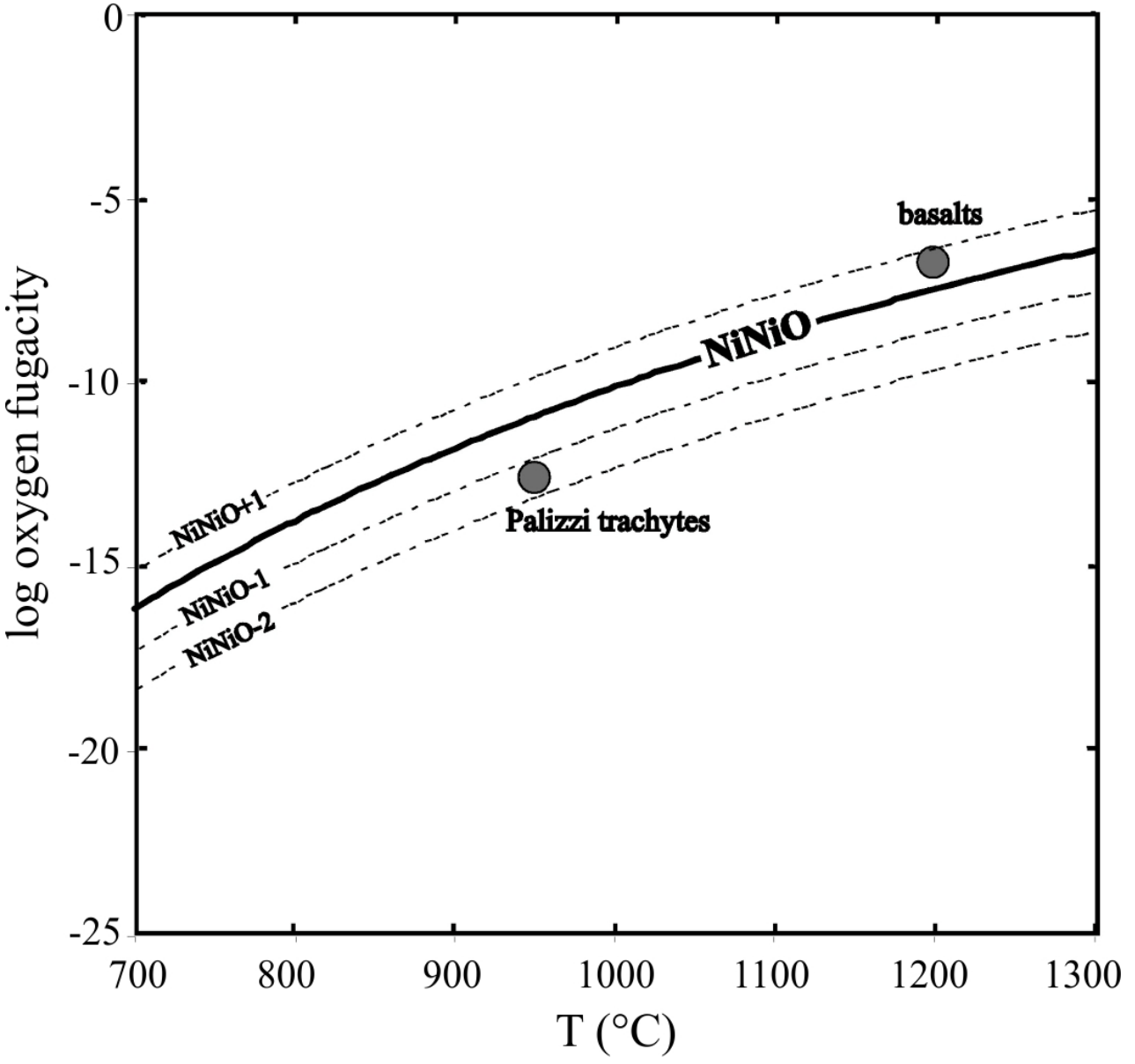
0
-5
-10
-15
-20
-25
log oxygen fugacity
700
800
900
1000
1100
1200
1300
T (°C)
basalts
NiNiO
Palizzi trachytes
NiNiO+1
NiNiO-1
NiNiO-2

Figure 8

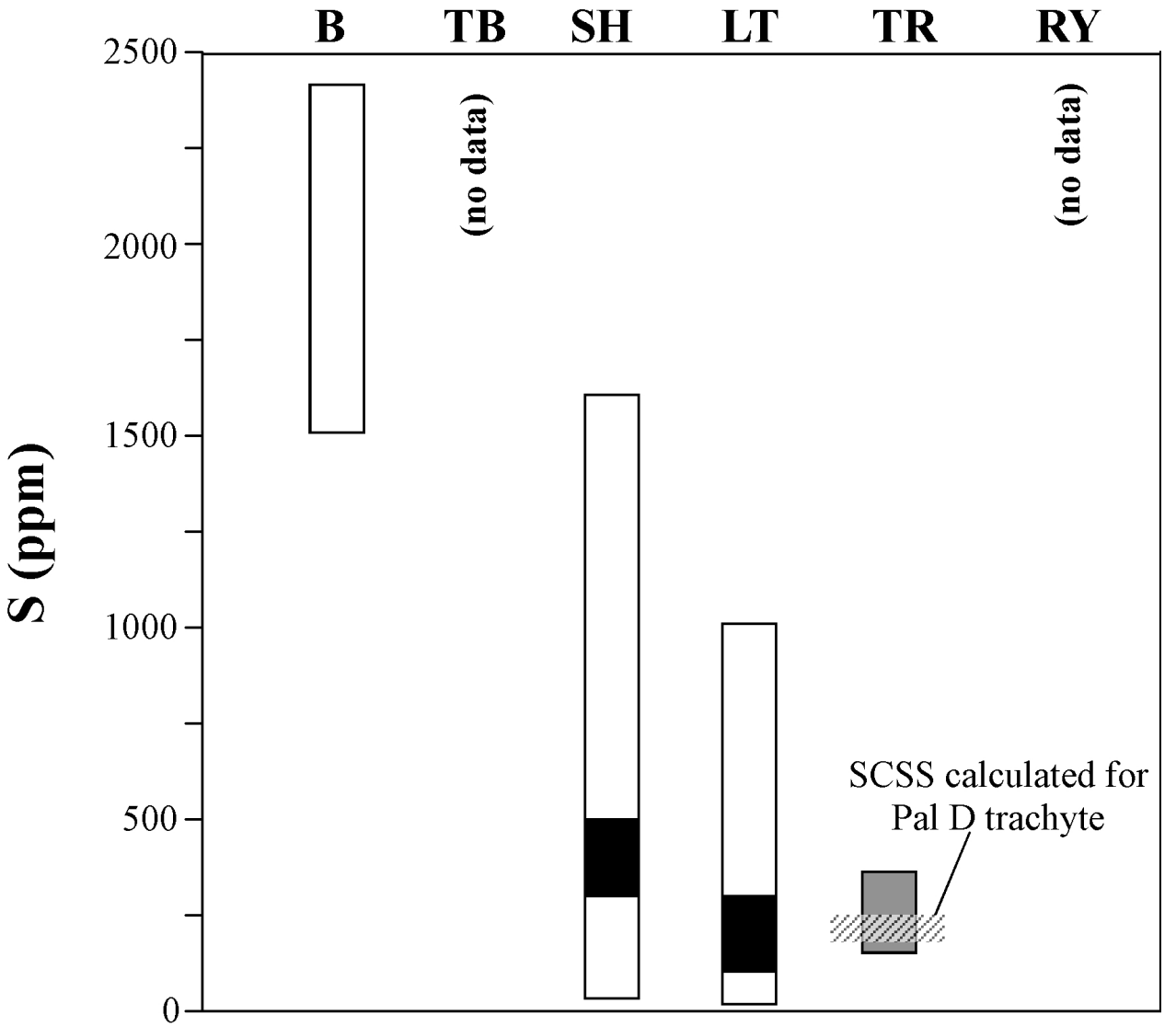
B
TB
SH
LT
TR
RY
2500
2000
1500
1000
500
0
S (ppm)
(no data)
(no data)
SCSS calculated for
Pal D trachyte

Figure 9

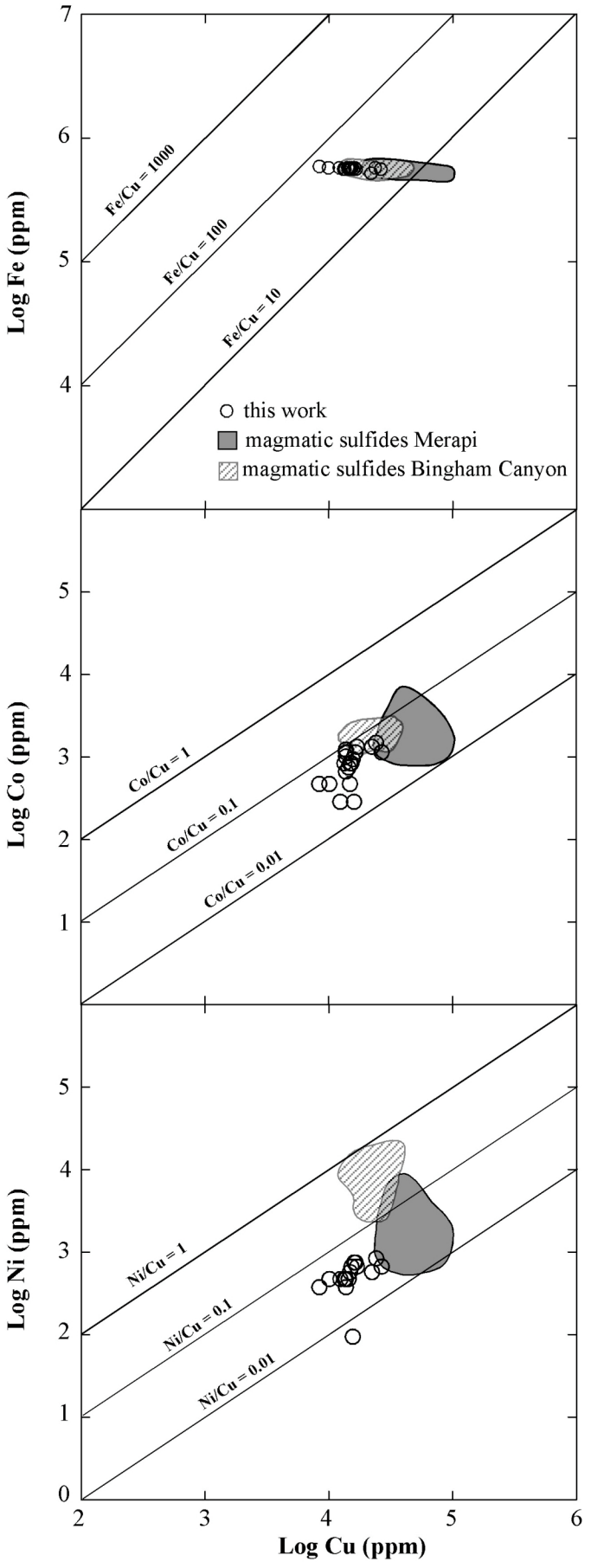
Log Fe (ppm)
Fe/Cu = 1000
Fe/Cu = 100
Fe/Cu = 10
this work
magmatic sulfides Merapi
magmatic sulfides Bingham Canyon
Log Co (ppm)
Co/Cu = 1
Co/Cu = 0.1
Co/Cu = 0.01
Log Ni (ppm)
Ni/Cu = 1
Ni/Cu = 0.1
Ni/Cu = 0.01
Log Cu (ppm)

Figure 10

Table 1. Representative (EPMA, wt%) analyses of phenocrysts of olivine (ol), clinopyroxene (cpx), plagioclase (pl), sanidine (sa) and biotite (bt) from Pal D trachyte; bdl: below detection limit.

Mineral	ol	cpx	cpx	pl	pl	pl	pl	sa	sa	bt	bt	bt	bt
Crystal	5	11	11	3	3	8	8	9	9	12	12	3	3
Position	core	core	rim	core	rim	core	rim	core	rim	core	rim	core	rim
SiO_2	36.47	51.40	50.80	55.78	56.38	55.49	55.27	63.80	61.84	36.40	35.54	36.54	36.20
TiO_2	0.04	0.38	0.61							6.27	5.92	5.81	5.96
Al_2O_3		2.33	3.09	25.92	26.19	27.39	26.56	19.04	19.52	14.02	13.86	13.97	13.88
FeOt	31.89	8.10	9.52	0.41	0.41	0.60	0.60	0.10	0.16	14.50	14.17	13.79	13.54
MnO	0.80	0.22	0.33							bdl	0.21	0.10	0.21
MgO	33.02	14.73	13.96							15.18	15.02	15.75	15.45
CaO	0.50	21.95	21.44	8.81	8.83	9.97	9.53	0.66	0.73				
Na_2O		0.44	0.52	6.59	6.54	6.68	6.00	4.13	3.86	0.89	0.60	0.84	0.59
K_2O		bdl	0.07	1.60	1.40	1.19	1.65	11.09	10.22	8.55	8.52	8.68	8.42
total	102.72	99.55	100.33	99.11	99.75	101.32	99.61	98.81	96.32	95.81	93.85	95.47	94.25
Fo	63.84												
Wo		43.78	44.39										
En		41.05	40.23										
Fs		15.17	15.38										
Mg# [(1)]		73.01	72.34										
An				38.88	39.54	42.45	42.64	3.09	3.66				
Ab				52.68	52.98	51.53	48.57	35.04	35.14				
Or				8.44	7.49	6.01	8.79	61.87	61.20				
Fe/(Fe+Mg)										0.35	0.35	0.33	0.33
T_{cryst} (°C)					910[(2)]		929[(2)]		765[(2)]	927[(4)]	931[(4)]	933[(4)]	931[(4)]
							924[(3)]		924[(3)]				

[(1)] Mg# = [100 x Mg/ (Mg + Fe)]. T_{cryst} (°C) = Temperature of crystallization. Thermometers utilized for calculation: [(2)] plagioclase- and alkali feldspar-liquid (Putirka, 2008; liquid composition is the average groundmass glass in Table 3); [(3)] two feldspars thermometer (Putirka, 2008); [(4)] Ti-in-phlogopite geothermometry (Righter and Carmichael, 1996).

Table 2. Electron microprobe analyses (wt %) of sulfide globules in the Pal D (trachyte) and Pal B (rhyolite) material. Two and, in one case, three analyses were carried out on large sulfides to check for homogeneity, and mean [n] and standard deviation (SD) are reported. bdl: below detection limit. bt: biotite; cpx: clinopyroxene; ol: olivine, pl: plagioclase; sa: sanidine; glomer: glomerophyre. Po formula: pyrrhotite chemical formula calculated from microprobe analysis of mineral major elements.

Sample	sulfide	host	size (μm)	mean [n] SD	Fe	S	Co	Mn	Ni	Zn	Cu	total	Po formula
Pal D													
PAL-90	90-13	cpx	25	mean [2]	58.32	37.85	0.10	0.08	0.00	0.05	1.50	97.88	$Fe_{0.94}S_{1.06}$
				SD	0.09	0.20	0.04	0.05	0.00	0.02	0.06	0.47	
PAL-90	90-14	cpx	20		53.30	39.64	0.14	0.09	0.06	bdl	2.16	95.39	$Fe_{0.87}S_{1.13}$
PAL-90	90-5	ol	30	mean [2]	59.07	37.84	0.09	0.15	0.07	bdl	1.48	98.70	$Fe_{0.95}S_{1.05}$
				SD	0.18	0.34	0.01	0.04	0.04	bdl	0.26	0.87	
PAL-90	90-4	glass	15		58.01	37.24	0.16	0.11	0.09	bdl	2.32	97.93	$Fe_{0.94}S_{1.06}$
PAL-90	90-2	cpx	35	mean [2]	59.51	38.07	0.05	0.10	0.04	0.06	0.80	98.63	$Fe_{0.95}S_{1.05}$
				SD	0.55	0.02	0.03	0.02	0.01	0.05	0.55	1.23	
PAL-15	15D 1	cpx	40		57.99	37.64	0.03	0.10	0.05	0.04	1.21	97.07	$Fe_{0.94}S_{1.06}$
PAL-15	15D-2	cpx	30		56.33	37.35	0.11	0.11	0.04	bdl	1.34	95.28	$Fe_{0.93}S_{1.07}$
PAL-15	15D-3	bt	20		57.60	37.53	0.12	0.13	0.05	bdl	1.32	96.75	$Fe_{0.94}S_{1.06}$
PAL-15	15D-4	mt	15		56.48	37.45	0.13	0.12	0.05	0.04	1.34	95.60	$Fe_{0.93}S_{1.07}$
PAL-15	15D-5	cpx	15		56.85	37.61	0.09	0.11	0.05	0.11	1.30	96.12	$Fe_{0.93}S_{1.07}$
PAL-90	U285-9	ol	5		57.09	38.05	0.07	0.10	0.04	0.11	1.34	96.80	$Fe_{0.93}S_{1.07}$
PAL-90	U297-10	mt	40		58.72	38.24	0.05	0.16	0.05	0.05	0.97	98.23	$Fe_{0.94}S_{1.06}$
PAL-90	U274	ol	30		57.19	37.24	0.14	0.18	0.07	0.07	1.62	96.52	$Fe_{0.94}S_{1.06}$
PAL-90	U293-17	mt	60	mean [2]	58.37	37.99	0.08	0.10	0.05	0.02	1.35	97.96	$Fe_{0.94}S_{1.06}$
				SD	0.31	0.37	0.01	0.02	0.06	bdl	0.05	0.84	
PAL-90	U297-18	pl	15		56.63	37.48	0.03	0.10	0.08	0.10	1.55	95.95	$Fe_{0.93}S_{1.07}$
PAL-15	U313-8	cpx	30	mean [2]	56.60	37.65	0.05	0.14	0.06	0.04	1.43	95.97	$Fe_{0.93}S_{1.07}$
				SD	0.77	0.03	0.01	0.01	bdl	bdl	0.58	1.40	
PAL-15	U317	glomer.	60	mean [3]	56.34	37.65	0.12	0.08	0.07	0.08	2.59	96.94	$Fe_{0.92}S_{1.08}$
				SD	0.06	0.02	0.04	0.06	0.03	0.02	0.12	0.34	
PAL-15	U316	cpx	20		57.96	37.57	0.12	0.11	0.08	0.04	1.58	97.46	$Fe_{0.94}S_{1.06}$
Pal B													
PAL-L	U298	sa	30	mean [2]	59.07	36.64	0.03	0.05	0.02	0.09	0.37	96.28	$Fe_{0.97}S_{1.03}$
				SD	0.71	0.11	0.01	0.03	0.02	bdl	0.06	0.95	

Table 3. Major element (wt.%), S, Cl and water content of melt inclusion (MI) of the Pal D pumice. Major elements, chlorine and sulfur by electron microprobe; water content by Raman spectroscopy (see Table 4 for the complete water content dataset). Mean and standard deviation (SD) of major element analyses of the glassy groundmass of Pal A and Pal D products are also reported; bdl: below detection limit; nd: not determined; bt: biotite; cpx: clinopyroxene, ol: olivine, pl: plagioclase.

MI	host	SiO_2	TiO_2	Al_2O_3	FeO tot	MnO	MgO	CaO	Na_2O	K_2O	P_2O_5	total	Cl ppm	S ppm	H_2O wt. %
42	px	58.55	0.82	17.45	5.42	0.18	1.41	2.68	5.49	6.38	bdl	98.37	4285	nd	nd
43	pl	59.54	0.39	17.50	4.72	0.21	1.16	2.65	5.74	7.02	0.38	99.33	2254	nd	nd
44	px	58.33	0.52	17.66	5.34	0.04	0.89	2.39	5.31	5.73	0.27	96.48	4104	nd	nd
45	bt	60.27	0.54	17.78	4.63	0.08	0.93	2.03	5.74	6.90	0.10	98.98	5196	nd	nd
46	ol	60.20	0.60	17.30	4.11	0.15	0.91	2.14	4.44	7.61	0.23	97.69	3820	320	nd
6	ol	59.84	0.61	17.34	4.08	0.13	0.86	2.26	4.42	7.77	0.25	97.54	3400	220	1.25
7	ol	59.94	0.54	17.46	4.19	0.11	0.94	2.17	4.60	7.60	0.19	97.74	3890	156	1.63
8	ol	61.57	0.55	17.62	3.92	0.13	0.82	2.19	4.58	7.67	0.24	99.29	4100	320	1.37
11	pl	60.42	0.40	18.68	3.27	0.05	0.68	2.97	4.56	6.99	0.19	98.20	3680	244	1.57
9	cpx	60.04	0.45	15.93	4.07	0.20	1.90	4.06	4.29	7.04	0.20	98.17	3630	320	1.70
41	cpx	60.18	0.46	17.03	3.79	0.10	0.87	2.16	4.32	7.45	0.23	96.58	4020	68	nd
20	cpx	61.62	0.57	17.57	4.18	0.09	0.88	2.08	3.67	7.49	0.20	98.35	3950	188	1.37
12	cpx	61.04	0.50	17.21	3.72	0.14	0.81	2.23	4.39	7.47	0.17	97.67	4090	188	1.80
14	cpx	60.38	0.54	17.40	4.75	0.10	0.94	2.41	4.41	7.61	0.24	98.80	3500	220	1.44
13	cpx	60.18	0.50	17.22	4.23	0.17	0.97	2.44	4.44	7.41	0.15	97.72	3790	208	1.32
15	cpx	59.79	0.61	16.16	4.49	0.13	1.88	3.88	4.13	7.19	0.19	98.45	3320	332	1.22
16	cpx	59.93	0.52	17.10	4.59	0.08	0.91	2.55	4.45	7.50	0.26	97.89	3980	232	1.33
3	bt	59.77	0.60	17.31	4.33	0.09	1.01	2.19	4.84	7.56	0.25	97.95	nd	376	1.43
Pal D groundmass glass															
Mean [19]		59.66	0.48	17.88	4.47	0.13	0.93	2.17	5.51	6.94	0.13	98.31	3290	nd	<1
SD		1.17	0.20	0.44	1.21	0.08	0.29	0.53	0.60	1.00	0.15	1.35	1343		
Pal A groundmass glass															
Mean [16]		56.91	0.61	17.49	6.52	0.13	1.87	4.32	4.74	6.82	0.60	100.0	3040	nd	nd
SD		0.64	0.04	0.21	0.22	0.03	0.25	0.49	0.17	0.20	0.06	0.32	300		

Table 4. Raman spectroscopy determination of H_2O content of melt inclusions (MI) and matrix glass of Pal D pumices; bt: biotite; cpx: clinopyroxene; ol: olivine, pl: plagioclase.

MI	Sample	MI/matrix	MI host	HW/LW*	H_2O wt%
1	PAL-15	matrix glass	-	0.43	0.39
2	PAL-15	matrix glass	-	0.66	0.61
3	PAL-15	MI	bt	1.56	1.43
4	PAL-15	MI	bt	2.74	2.52
5	PAL-15	matrix glass	-	0.72	0.66
6	PAL-15	MI	ol	1.36	1.25
7	PAL-15	MI	ol	1.77	1.63
8	PAL-15	MI	cpx	1.48	1.37
9	PAL-15	MI	cpx	1.85	1.70
10	PAL-15	MI	pl	1.33	1.23
11	PAL-15	MI	pl	1.71	1.57
12	PAL-15	MI	cpx	1.96	1.80
13	PAL-15	MI	cpx	1.44	1.32
14	PAL-15	MI	cpx	1.56	1.44
15	PAL-15	MI	cpx	1.33	1.22
16	PAL-15	MI	cpx	1.44	1.33
17	PAL-15	MI	pl	1.39	1.28
18	PAL-15	matrix glass	-	0.86	0.79
19	PAL-15	MI	pl	1.50	1.38
20	PAL-15	MI	pl	1.49	1.37
21	PAL-15	MI	pl	1.61	1.48
22	PAL-90	MI	cpx	1.09	1.01
23	PAL-90	MI	bt	1.80	1.66
24	PAL-90	MI	cpx	2.06	1.90
25	PAL-90	MI	bt	1.80	1.66
26	PAL-90	embayment	bt	1.06	0.98
27	PAL-90	MI	bt	2.19	2.02
28	PAL-90	MI	bt	1.59	1.46
29	PAL-90	MI	cpx	1.86	1.71
30	PAL-90	MI	cpx	1.93	1.77
31	PAL-90	MI	bt	1.84	1.69
32	PAL-90	MI	bt	1.56	1.44
33	PAL-90	MI	ol	1.42	1.30
34	PAL-90	MI	bt	1.75	1.61
35	PAL-90	MI	bt	1.91	1.76
36	PAL-90	MI	cpx	1.93	1.78
37	PAL-90	MI	ol	1.23	1.13
38	PAL-90	MI	bt	2.43	2.24
39	PAL-90	embayment	bt	1.96	1.80
40	PAL-90	embayment	bt	1.59	1.47

*Calculated area ratio between the water (HW) and silicate (LW) bands (for details see Di Genova et al., 2017).

Table 5. Compositional data (MgO wt% and dissolved S in melt inclusions) and summary of the chemical-physical parameters of Pal D trachytic magma measured or calculated in this work (see text for explanation), for La Sommata basalt and for La Fossa rhyolite. MI: melt inclusions; SCSS: sulfur concentration at sulfide saturation.

	MgO (bulk rock, wt%)	S in silicate melt (MI mean, ppm)	T (°C)	P (MPa)	ΔNNO	log fS_2 (bar)	a_{FeS}	SCSS (ppm)	Cl solubility (wt.%)
Sommata	8.34[(1)]	2300[(1)]	1180[(1)]	100-300[(2)]	+0.72[(3)]	-1.4[(4)]	-1.1/-2[(4)]	-	~4
Pal D	1.25-1.96	160-380	907-968	30-54	-1/-2	-4.5	~1	200-250	~1
La Fossa rhyolite	0.14[(1)]	<100[(1)]	750-850[(5)]	30-54[(6)]	-	-	-	-	~0.5

[(1)] Gioncada et al. (1998); [(2)] calculated from H_2O content of melt inclusions from Gioncada et al. (1998) and Le Voyer et al. (2014); [(3)] Métrich and Clocchiatti (1996); [(4)] Scaillet and Pichavant (2005); [(5)] assumed T for a rhyolitic magma; [(6)] assumed same as Pal D